Accepted for Publication in the Astrophysical Journal

The Dark Molecular Gas

Mark G. Wolfire

Department of Astronomy, University of Maryland, College Park, MD 20742-2421

mwolfire@astro.umd.edu

David Hollenbach

SETI Institute, 515 N. Whisman Road, Mountain View, CA 94043

dhollenbach@seti.org

and

Christopher F. McKee

Physics Department and Astronomy Department, University of California at Berkeley, Berkeley, CA 94720

cmckee@astron.berkeley.edu

ABSTRACT

The mass of molecular gas in an interstellar cloud is often measured using line emission from low rotational levels of CO, which are sensitive to the CO mass, and then scaling to the assumed molecular hydrogen H_2 mass. However, a significant H_2 mass may lie outside the CO region, in the outer regions of the molecular cloud where the gas phase carbon resides in C or C^+. Here, H_2 self-shields or is shielded by dust from UV photodissociation, whereas CO is photodissociated. This H_2 gas is "dark" in molecular transitions because of the absence of CO and other trace molecules, and because H_2 emits so weakly at temperatures 10 K $< T <$ 100 K typical of this molecular component. This component has been indirectly observed through other tracers of mass such as gamma rays produced in cosmic ray collisions with the gas and far-infrared/submillimeter wavelength dust continuum radiation. In this paper we theoretically model this dark mass and find that the fraction of the molecular mass in this dark component is remarkably constant (~ 0.3 for average visual extinction through the cloud $\bar{A}_V \simeq 8$) and

insensitive to the incident ultraviolet radiation field strength, the internal density distribution, and the mass of the molecular cloud as long as $\bar{A}_V$, or equivalently, the product of the average hydrogen nucleus column and the metallicity through the cloud, is constant. We also find that the dark mass fraction increases with decreasing $\bar{A}_V$, since relatively more molecular H_2 material lies outside the CO region in this case.

Subject headings: ISM: clouds

1. INTRODUCTION

Various observations have indicated that a substantial amount of interstellar gas exists in the form of molecular hydrogen (H_2) along with ionized carbon (C^+), but little or no carbon monoxide (CO). The total mass in molecular hydrogen has been estimated from gamma ray observations from COS-B (Bloemen et al. 1986) and EGRET (Energetic Gamma Ray Experiment Telescope) (Strong & Mattox 1996) and analysis of this data showed more gas mass than can be accounted for in H I and CO alone (Grenier et al. 2005). In addition, the dust column density maps of the Galaxy from DIRBE, and maps of the 2MASS J-K extinction show additional gas not seen in H I or CO (Grenier et al. 2005) and is presumably molecular hydrogen. In molecular line observations and modeling of low column density molecular clouds the H_2/CO ratio is found to be variable and much larger than 10^4 so that only a small fraction of the C is in CO with the remainder presumably in C^+ (Hollenbach et al. 2009; Goldsmith et al. 2008). Reach et al. (1994) using infrared continuum maps of diffuse clouds along with H I and CO observations, found H_2 masses comparable to the H I masses, with only small amounts of CO. A mixture of H_2 and C^+ is also inferred to exist in diffuse clouds where the H_2 and CO columns are measured by UV absorption spectroscopy and the CO accounts for only a trace amount of C (Sonnentrucker et al. 2007; Burgh et al. 2007; Sheffer et al. 2008). This component of the interstellar medium (ISM), termed "dark gas" by Grenier et al. (2005), is also inferred to exist in extragalactic observations comparing far-infrared and CO mass estimates especially in low metallicity galaxies (Israel 1997; Leroy et al. 2007).

Such an H_2 and C^+ layer is also predicted from theoretical models of diffuse gas (van Dishoeck & Black 1988) and surfaces of molecular clouds (Tielens & Hollenbach 1985) that indicate the transition from C^+ to CO is deeper into the cloud than the transition from H to H_2. Essentially, the theoretical models show that H_2 self-shields itself from UV photodissociation more effectively than CO. This layer is "dark" in rotational H_2 transitions primarily because the ground state transition 0-0 S(0) at 28 μm lies about $\Delta E/k \simeq 512$ K

above ground; at the temperatures 10 K $< T <$ 100 K typical of the dark component the fluxes from the H_2 rotational transitions lie below current sensitivities. This layer is dark in CO because of its very low abundance. Although the dark gas layer is "dark" in H_2 and CO, it does emit mainly in [C II] 158 μm fine-structure line emission. In preliminary estimates (M. Wolfire et al. 2010, in preparation) the calculated local Galactic [C II] emission from the WIM and CNM (diffuse phases that are not associated with molecular clouds) underestimate the COBE observations of the line emission in the plane by a factor of 1/3 to 1/2 and could be another indicator of dark gas. Similarly, Shibai et al. (1991) and Cubick et al. (2008) found the bulk of the [C II] emission in the Galactic plane seen by BIRT and COBE arises in neutral gas associated with molecular clouds.

In this paper we present models of molecular cloud surfaces to estimate the mass of gas in the "dark" component. In §2 we discuss modifications to existing photodissociation region (PDR) codes, and the modeling procedure. In §3 we define the dark gas mass fraction and other parameters used in our models, discuss the average gas density distribution assumed in our modeling, and derive an expression for the dark gas fraction in terms of parameters found in our numerical modeling procedure. The modeling results start in §4 with a simple isobaric cloud model in the limit of clumps that are optically thin to the incident radiation field, resulting in an estimate of the dark gas fraction for a typical giant molecular cloud. We then in §5 enhance this model with the inclusion of turbulent pressure and find the dark gas fraction as a function of incident field strength and cloud mass. We also discuss the variation in the dark gas fraction as a function of metallicity (over a limited range), the average hydrogen column through a cloud, the average visual extinction through a cloud, and the opacity of the clumps. We compare our results with observations. Finally, in §6 we conclude with a discussion and summary.

2. Models

Our goal is to determine the mass in the C^+/H_2 layer—the dark gas—in molecular clouds. Our analysis is based in part on the results of a modified version of the photodissociation region (PDR) code of Kaufman et al. (2006). In applying this code, we are making four main approximations: First, we assume that the inhomogeneities in actual molecular clouds can be approximated as clumps of density n_c occupying a fraction f_V of the volume; we neglect the interclump medium, so that the locally volume-averaged density, $\bar{n}$ is given by $\bar{n} = f_V n_c$. Second, we assume that these clumps are optically thin to UV radiation; as a result, the radiative transfer is the same as that in a homogeneous medium with the mean density, $\bar{n}$. The validity of this assumption is discussed in §5.4 below, where we show

that even in the limit of very optically thick clumps, our models give essentially the same dark gas mass fraction. Third, in the PDR solution to the variation with depth of chemical abundances and gas temperature, we assume that the layer of dark gas is not geometrically thick, so that we can apply the results of a 1D slab model to the spherical problem. However, in calculating the mass of gas in the dark gas layer, we do take into account the spherical geometry. Fourth, we assume that we can calculate the chemical abundances in steady state. This assumption is discussed in §5.5 after we have derived densities, turbulent speeds and characteristic distances. With these approximations, the physical conditions and chemical abundances within the cloud are a function of the optical depth from the cloud surface and we can apply a single, one-dimensional PDR model to a continuous density distribution in which the gas density n_c inside the clumps can vary as a function of the distance r of a clump from the center of the GMC.

The PDR models find the gas temperature in thermal balance and the chemical equilibrium abundance of all dominant atomic and molecular species as a function of depth into a gas layer. The models require the incident far-ultraviolet (FUV; 6 eV $< h\nu <$ 13.6 eV) radiation, extreme ultraviolet (EUV, 13.6 eV $< h\nu \lesssim$ 100 eV) radiation, soft X-ray (100 eV $\lesssim h\nu \lesssim$ 1 keV) radiation, cosmic-ray flux, and either the spatial distribution in density or the spatial distribution in thermal pressure. If the density distribution is provided, the code will iterate on the gas temperature at fixed density until thermal balance is achieved. If the thermal pressure ($P_{\rm th}/k = n_t T$, where n_t is the total particle density) is provided, the code will iterate on both the density and temperature. With these inputs, the temperature, and the atomic and molecular abundances are calculated self-consistently.

2.1. Modified PDR Code

The PDR code of Kaufman et al. (2006) is based on two main parts. The first part is derived from Kaufman et al. (1999), Wolfire et al. (1990), and Tielens & Hollenbach (1985) models and is the main program for calculating the chemistry, thermal balance, and line emission. The second part is based on the Le Petit et al. (2006) Meudon PDR code and is used for all of the molecular hydrogen processes. The Kaufman et al. (2006) code assumes a 1D UV flux normal to the cloud surface. Here we consider the average radiation field produced by all OB associations illuminating the giant molecular cloud (GMC) and the field at the cloud surface is expected to be relatively isotropic over 2π steradians. In order to account for the isotropic field, we assume a 1D flux incident at an angle of 60 degrees to the normal. This unidirectional field has the same flux normal to the cloud surface as the isotropic field, and thus the same energy input to the cloud, and it more closely approximates

the depth penetration of the field. The photo rates are modified to account for twice the path length of the incident field for a given A_V measured normal to the surface. In the Meudon portion of the code, the isotropic field is accounted for explicitly in the depth dependence of the photo rates.

We have also included several changes in the elemental abundances and chemical network that affect the carbon chemistry. We adopt the gas phase carbon abundance $\mathcal{A}_{\rm C} = 1.6 \times 10^{-4}$ from Sofia et al. (2004), where $\mathcal{A}_{\rm C} = n_{\rm C}/n$ and where $n_{\rm C}$ is the gas phase number density of elemental carbon and n is the number density of H nuclei. We also include the C^+ radiative and dielectronic recombination rates from Badnell (2006a) and (Badnell 2006b)[1], who have found that the rates at low temperatures can be a factor of 2-3 higher than was used in the past (e.g., Nahar & Pradhan 1997). Another change in the chemical network is to include OH production on grains from Hollenbach et al. (2009). We adopt the fastest possible rate, having each collision of O with a grain combine with H and produce OH. This limit tends to maximize CO production and minimize the dark gas fraction. We also include the ion-dipole reaction rates for C^+, H_3^+, and He^+, reacting with OH and H_2O as discussed in Hollenbach et al. (2009).

2.2. External Radiation Field

The external fluxes of FUV radiation, EUV/soft X-ray radiation, and cosmic rays are model inputs and must be specified. Associations produce bright photodissociation regions on nearby cloud surfaces. For example, the Trapezium cluster in Orion produces the bright Orion PDR on cloud surfaces only ~ 0.1 pc distant. As an association evolves, the Strömgren region expands, the embedded H II region breaks out of the cloud, the resultant champagne flow and blister evaporation disperses the cloud and the distance between the cloud and association increases, thus allowing more of the cloud to be illuminated than the initial hot spot. The combination of cloud and association evolution, the distribution of associations around the cloud, and the continuous formation of new associations, elevates the average radiation field illuminating the cloud to a field strength that is greater than the average interstellar radiation field. A detailed evaluation of this process is presented in Wolfire, Hollenbach, & McKee (2010, in preparation). They find the average field incident on clouds is on the order of ~ 20 times higher than the local Galactic interstellar field. We adopt the Draine (1978) interstellar radiation field that is equal to ~ 1.7 times the Habing (1968) local interstellar field (1.6×10^{-3} erg cm^{-2} s^{-1} for FUV photons). We also use the notation

[1]http://amdpp.phys.strath.ac.uk/tamoc/DR

that G_0 is the radiation field in units of the Habing field and G'_0 is the field relative to the local Galactic field found by Draine (1978), so that $G'_0 = G_0/1.7$. To clarify the definition of G'_0, which is consistent with the original definition given in Tielens & Hollenbach (1985), G'_0 is the ratio of the photorates at the surface ($A_V = 0$) of our cloud to the same rates in the Draine field in free space. Thus, $G'_0 = (2\pi I)/(4\pi I_D) = 0.5I/I_D$, where I is our incident isotropic intensity and $I_D = 2.2 \times 10^{-4}$ erg cm^{-2} s^{-1} sr^{-1} is the Draine intensity for the local ISM.[2] Here we examine a range of FUV fields, $3 < G'_0 < 30$, consistent with (and generously encompassing) the results of Wolfire et al. (2010). Throughout this paper we simply scale the flux by G'_0 and keep the spectral energy distribution fixed as given by the Draine (1978) field.

As discussed in Wolfire et al. (2003), the soft X-ray/EUV flux from the diffuse interstellar field can be produced by a combination of supernova remnants and stellar sources. The field shining on the molecular cloud can be enhanced above the interstellar flux due to the OB associations near the molecular cloud. We assume that we are outside any of the H II regions associated with the OB associations, and simply scale the soft X-ray/EUV flux by the same factor that we do for the effective far-ultraviolet radiation field $\zeta'_{\rm XR} = G'_0$. A corollary of this assumption is that the fraction of gas that is ionized is negligible. Wolfire et al. (2003) adopted a standard soft X-ray/EUV shielding column of neutral gas of column density $N = 1 \times 10^{19}$ cm^{-2}. The layer $N < 10^{19}$ cm^{-2} mainly consists of WNM gas photoevaporated from the molecular and CNM clump surfaces and does not provide significant shielding to the FUV photodissociating radiation field. We are mainly concerned with the deeper layers and assume that the clouds are shielded by a column of this order. As we shall demonstrate in §5, the absorption of X-ray/EUV radiation at columns in the range 10^{19} cm$^{-2} < N \sim 10^{21}$ cm^{-2} leads to a drop in the thermal pressure by a factor of ~ 10 in the H I layer in the cloud.

The cosmic-ray flux is also associated with massive star evolution, but is not as likely to be simply proportional to G'_0 as for the EUV/soft X-ray flux. Since the temperatures of cloud interiors do not exceed $T = 10 - 20$ K, the cosmic ray flux in cloud interiors cannot be higher than a factor of $\sim 2 - 3$ times the diffuse ISM value or else the heating rate would push internal cloud temperatures higher than observed. In most of our calculations, we therefore assume that cosmic-ray rates are not enhanced by the nearby molecular cloud OB associations.

The cosmic ray rate can also affect the formation of CO in the diffuse gas and outer

[2]Note that an opaque cloud in the local ISRF therefore experiences $G'_0 = 0.5$, since the molecule at the surface is only illuminated from 2π sterradians.

molecular cloud layers through the production of OH as discussed by van Dishoeck & Black (1986, 1988). There are several observations, mainly of H_3^+, that indicate higher cosmic ray ionization rates by a factor of ~ 10 along select lines of sight in the diffuse ISM (Indriolo et al. 2007); however the H_3^+ observations do not indicate higher cosmic ray rates in the denser, molecular clouds considered here (McCall et al. 1999). We adopt our standard rate for the majority of this paper, but consider the effects of higher cosmic ray rates in the outer portions of the cloud in §5.2.6,

3. Density Distribution and Dark-Gas Fraction

To estimate the dark-gas fraction in a molecular cloud, we assume that it is spherical. Let $R_{\rm CO}$ be the radius of the CO part of the cloud, defined by the condition that the optical depth from $R_{\rm CO}$ to the surface in the $J = 1 - 0$ transition is $\tau_{\rm CO} = 1$. Let $R_{\rm H_2} > R_{\rm CO}$ be the radius of the part of the cloud in which hydrogen is molecular; we define this as the radius at which the mass density in H_2 molecules equals that in H atoms. Finally, the total cloud radius, $R_{\rm tot}$, includes the H I shielding layer that absorbs the FUV radiation incident upon the cloud, enabling the gas to become molecular. The corresponding masses are the CO cloud mass, $M(R_{\rm CO})$, the total molecular mass, $M(R_{\rm H_2})$, and the total cloud mass, $M(R_{\rm tot})$, respectively, including the associated helium. The dark gas extends from $R_{\rm CO}$ to the atomic-molecular transition radius at $R_{\rm H_2}$. The dark-gas mass fraction is then

$$f_{\rm DG} = \frac{M(R_{\rm H_2}) - M(R_{\rm CO})}{M(R_{\rm H_2})}. \tag{1}$$

Note that $f_{\rm DG}$ is the fraction of *molecular* (H_2) gas (and not the fraction of the total mass, atomic plus molecular) that is dark. It is also not the ratio of the dark gas to the gas in the CO zone.

The gas in the cloud generally has large density fluctuations. In the H I, this is because the gas can exist in two distinct phases, cold ($T \sim 10^2$ K) and dense, and warm ($T \sim 10^4$ K) and tenuous (e.g., Wolfire et al. 2003), whereas the molecular gas is generally supersonically turbulent (Larson 1981) and therefore has large density variations. Let $n(\mathbf{r})$ be the density of H nuclei at a point in the cloud, and let $\bar{n}(r)$ be the locally volume-averaged density at that radius in the cloud. Following Larson (1981), we assume that $\bar{n}(r) \propto 1/r$. This corresponds to a global column density that is independent of radius,

$$\bar{N} \equiv \frac{M(r)}{\mu_{\rm H}\pi r^2} = 2r\bar{n}(r) = {\rm const}, \tag{2}$$

where $\mu_{\rm H} = 2.34 \times 10^{-24}$ g is the mass per H nucleus. For numerical evaluation, we usually use a column density $\bar{N} = 1.5 \times 10^{22}$ cm^{-2} from Solomon et al. (1987). The column $\bar{N}$

corresponds to an average visual extinction $\bar{A_V}$ through the cloud given by

$$\bar{A_V} = \frac{\bar{N} Z'}{1.9 \times 10^{21} \text{ cm}^{-2}} \equiv \frac{\bar{N}}{N_0} = 5.26 \bar{N}_{22} Z', \tag{3}$$

where $N_0 = 1.9 \times 10^{21} Z'^{-1}$ cm^{-2} is the radial column density corresponding to a visual extinction of unity (Bohlin et al. 1978; Rachford et al. 2002), $\bar{N}_{22} \equiv \bar{N}/(10^{22} \text{ cm}^{-2})$, $Z' \equiv Z/Z_\odot$ is the metallicity relative to solar, and assuming that the gas to dust ratio is constant within the cloud and the dust opacity scales with the gas metallicity Z'. The relation between the mass and the locally volume-averaged density is

$$\bar{n}(r) = 30.4 \, \frac{\bar{N}_{22}^{3/2}}{M_6(r)^{1/2}} \quad \text{cm}^{-3}, \tag{4}$$

where $M_6(r) \equiv M(r)/(10^6 \, M_\odot)$.

The PDR code is run for a cloud of mass $M(R_{\rm CO})$ on a grid of visual extinction, A_V, measured from the surface of the cloud at $R_{\rm tot}$ to a point r inside the cloud. We denote the corresponding column density as

$$N(r) \equiv - \int_{R_{\rm tot}}^{r} \bar{n} dr' \tag{5}$$

to distinguish it from the globally averaged value in equation (2). Note that $N(r)$ is the column density *outside* of r, whereas $\bar{N}$ is the average column density through the cloud and does not depend on r for our $1/r$ average density distribution. The visual extinction A_V corresponding to a column density N is given as in equation (3) with $\bar{N}$ replaced by N. Note that the column density, N (or extinction, A_V) between $R_{\rm CO}$ and $R_{\rm tot}$ is not known *a priori* and is one of the main results of our calculation. In addition, for a $1/r$ mean density distribution, the column through the cloud center is infinite, but the total mass within the $\tau_{\rm CO} = 1$ surface is well defined and is one of the input parameters. In practice we run the PDR model to a depth of $A_V = 10$ and adjust the inner radius of our grid at $A_V = 10$ so that the integrated CO cloud mass, $M(R_{\rm CO})$, is the input value. Our results do not depend on the value of A_V we choose for the inner radius since there is so little mass or radius contained in the small central region where the radial A_V goes to infinity as r goes to zero.

The results from the PDR code determine both the extinction at the H I – H_2 interface, $A_V(R_{\rm H_2})$ and the extinction at the surface of the CO cloud, $A_V(R_{\rm CO})$. The difference between these gives the extinction of the dark-gas layer,

$$\Delta A_{V,\,\rm DG} \equiv A_V(R_{\rm CO}) - A_V(R_{\rm H_2}). \tag{6}$$

For a cloud with an r^{-1} density profile, corresponding to $M(r) \propto r^2$, the dark-gas mass fraction is

$$f_{\rm DG} = 1 - \left(\frac{R_{\rm CO}}{R_{\rm H_2}}\right)^2, \quad (7)$$

$$= 1 - \exp\left(-\frac{4N_0\Delta A_{V,\,\rm DG}}{\bar{N}}\right), \quad (8)$$

$$= 1 - \exp\left(\frac{-0.76\Delta A_{V,\,\rm DG}}{Z'\bar{N}_{22}}\right) \quad (9)$$

$$= 1 - \exp\left(\frac{-4.0\Delta A_{V,\,\rm DG}}{\bar{A}_V}\right). \quad (10)$$

This result is generalized to other density profiles in Appendix A. The dark-gas fraction thus depends upon only two quantities, the radial column density of the dark-gas layer, $\Delta N = N_0\Delta A_{V,\,\rm DG}$, and the mean column density of the cloud, $\bar{N}$. When expressed in terms of the extinction of the dark gas layer, $\Delta A_{V,\,\rm DG}$, a dependence on the metallicity, Z', also enters. Perhaps most simply, when expressed in terms of $\Delta A_{V,\,\rm DG}$ and $\bar{A}_V$, the fraction depends only on the ratio $\Delta A_{V,\,\rm DG}/\bar{A}_V$. This is intuitive since (discussed later in detail), $\Delta A_{V,\,\rm DG}$ is a measure of the dark gas mass and $\bar{A}_V$ is a measure of the molecular mass.

4. Radiatively Heated Clumps at Constant Pressure

As a first step, we consider the case of isobaric clumps with a thermal pressure that is independent of position within the cloud. The clumps are heated by an FUV/soft X-ray radiation field that is attenuated by the gas between the clumps and the surface of the PDR, plus a column of 10^{19} cm^{-2}. (The clumps are also heated by the cosmic rays, but this heating is generally less important in the dark-gas region.) The thermal pressure is $P_{\rm th} = x_t n_c kT$, where x_t is the sum over the abundances of all species relative to hydrogen nuclei, $x_t = \Sigma_i n_i/n$; for atomic gas $x_t \simeq 1.1$, while for molecular gas $x_t \approx 0.6$. Note that the density derived from the isobaric PDR model is n_c, the density of the cold ($T \lesssim 300$ K) gas component. We assume that warm ($T \sim 8000$ K) H I at the same thermal pressure fills the remaining space, but we assume that this has a negligible fraction of the mass. As noted in §2 above, the volume filling factor is given by $f_{\rm V}(r) = \bar{n}(r)/n_c(r)$, where $\bar{n}(r)$ is the locally volume-averaged H nucleus density (i.e., the density at r averaged over the clumps since we are neglecting the interclump medium) and $n_c(r)$ is the H-nucleus density of the cold (clump) gas.

The model outputs include the local density in the clumps, $n_c(r)$, the volume filling factor of the clumps, $f_{\rm V}$, the fraction of atomic hydrogen, $x_{\rm HI} = n_{\rm HI}/n_c$, and the fraction of

molecular hydrogen, $x_{\rm H_2} = n_{\rm H_2}/n_c = \frac{1}{2}(1 - x_{\rm HI})$ as functions of extinction from the surface of the cloud, A_V. The total mass in each component is found by integrating the density distributions

$$M(R_{\rm H_2}) = \int_0^{R_{\rm tot}} 2\mu_{\rm H}\, x_{\rm H_2}(r') n_c(r') f_{\rm V}(r') 4\pi r'^2\, dr' \quad , \tag{11}$$

$$M(R_{\rm CO}) = \int_0^{R_{\rm CO}} 2\mu_{\rm H}\, x_{\rm H_2}(r') n_c(r') f_{\rm V}(r') 4\pi r'^2\, dr' \quad , \tag{12}$$

where $R_{\rm CO}$ is the radius of the $\tau_{\rm CO} = 1$ surface, and $R_{\rm tot}$ is the outer radius of the entire cloud, which includes (from center outwards) the CO region, the region with H_2 and C^+, and the outer atomic envelope with atomic H and C^+ (see Fig. 1 for an illustration of the various radii and optical depths). Note that $R_{\rm CO}$ is an input to our model while $R_{\rm tot}$ is an output; it is the outer radius that gives just enough shielding such that CO J=1-0 becomes optically thick at $R_{\rm CO}$.

We have run cases for a representative cloud of mass $M(R_{\rm CO}) = 1 \times 10^6\ M_\odot$, with incident radiation fields $G_0' = \zeta_{\rm XR}' = 10$, and two fixed values of the pressure, $P_{\rm th}/k = 10^4$ K cm^{-3} and 10^5 K cm^{-3}, which covers the observed range of thermal pressure deduced from ^{12}CO and ^{13}CO observations of molecular clouds in the Galactic plane (Sanders et al. 1993). For $P_{\rm th}/k = 10^4$ K cm^{-3}, the atomic-molecular transition occurs at $A_V(R_{\rm H_2}) = 0.54$, the transition to optically thick CO (at $\tau_{\rm CO} = 1$) occurs at $A_V(R_{\rm CO}) = 1.2$, and the dark-gas fraction is found to be $f_{\rm DG} = 0.28$. The total molecular mass is related to $M(R_{\rm CO})$ by

$$M(R_{\rm H_2}) = \frac{M(R_{\rm CO})}{1 - f_{\rm DG}} \ , \tag{13}$$

with $M(R_{\rm H_2}) = 1.4\, M(R_{\rm CO})$ in this case. For $P_{\rm th}/k = 10^5$ K cm^{-3}, we find $A_V(R_{\rm H_2}) = 0.10$, $A_V(R_{\rm CO}) = 0.86$, $f_{\rm DM} = 0.31$ and $M(R_{\rm H_2}) = 1.4\, M(R_{\rm CO})$. Although the transitions to H_2 and CO gas are shifted to lower column densities for the $P_{\rm th}/k = 10^5$ K cm^{-3} case, the dark-gas faction remains relatively unchanged.

To investigate the sensitivity of this result to variations in the density distribution and FUV radiation fields, we have constructed more realistic cloud models that include the effects of a two-phase thermal pressure and the effects of turbulence.

5. Clumps in a Turbulent, Two-Phase Medium

The illumination of the cloud by X-ray/EUV and FUV radiation will heat and evaporate the clumps, leading to a two-phase region in the outer regions of the molecular cloud consisting of warm $T \sim 8000$ K interclump gas and cooler $T \lesssim 300$ K clumps. We assume

the two-phase thermal pressure is the geometric mean of the minimum and maximum thermal pressures allowed for a two-phase medium, $P_{\rm th}^{\rm 2p} = (P_{\rm max}P_{\rm min})^{1/2}$, and we again assume that the mass of the interclump gas is negligible. Shocks or turbulence will tend to keep the thermal pressure above $P_{\rm min}$, while condensation of WNM into CNM will tend to keep the thermal pressure below $P_{\rm max}$. The geometric mean is roughly consistent with the mean thermal pressure in cold gas found in numerical simulations of two-phase ISM disks with turbulence (Piontek & Ostriker 2007). For sufficiently strong external radiation fields, photoevaporation of the cool clumps near the outer boundary of the cloud increases the density (and therefore the thermal pressure) of the all-pervasive interclump medium, so that the thermal pressure due to radiative heating exceeds the turbulent pressure there. However, the thermal pressure due to radiative heating drops from the cloud surface inward due to absorption of the soft X-ray/EUV and FUV radiation.

For sufficiently weak radiation fields such as exist in the interior regions of molecular clouds, most of the gas is cold and the turbulent motions are very supersonic, which generates a wide range of thermal pressures. Both observational (Lombardi et al. 2006; Ridge et al. 2006) and theoretical (Vazquez-Semadeni 1994; Ostriker et al. 2001) studies suggest that turbulent clouds have a log-normal density distribution that applies to the dense component in the two-phase medium (Audit & Hennebelle 2010). The mass-weighted median density, $\langle n\rangle_{\rm med}$, in this turbulent medium is related to the volume-averaged density, $\bar{n}$, by

$$\langle n\rangle_{\rm med} = \bar{n}\exp(\mu)\ , \tag{14}$$

where

$$\mu \approx 0.5\ln(1+0.25\mathcal{M}^2)\ , \tag{15}$$

(Padoan et al. 1997), $\mathcal{M} = \sqrt{3}\sigma/c_s$ is the 3D Mach number, σ is the 1D velocity dispersion, and $c_{\rm s}$ is the sound speed. The typical thermal pressure in a turbulent medium is $P_{\rm th}^{\rm turb} = x_t\langle n\rangle_{\rm med}kT$: half the mass is at a greater thermal pressure than this and half at a lower one. To treat the complex situation in which both radiative heating and turbulence determine the pressure, we assume that the typical thermal pressure in the gas is the larger of that due to radiative heating, $P_{\rm th}^{\rm 2p}$, and that due to turbulence, $P_{\rm th}^{\rm turb}$,

$$P_{\rm th} = \max\left(P_{\rm th}^{\rm 2p}, P_{\rm th}^{\rm turb}\right). \tag{16}$$

To determine the Mach number, we note that the relation between the linewidth and size of a cloud is given by the identity

$$\sigma(r) = 0.52\left[\alpha_{\rm vir}\left(\frac{\Sigma}{10^2\ M_\odot\ {\rm pc}^{-2}}\right)\left(\frac{r}{\rm pc}\right)\right]^{1/2}\quad {\rm km\ s^{-1}}, \tag{17}$$

where $\alpha_{\rm vir} \equiv 5\sigma^2 r/GM$ is the virial parameter and $\Sigma \equiv M/\pi r^2 = \mu_{\rm H}\bar{N}$ is the average mass surface density of the cloud (see eq. 27 in McKee & Ostriker 2007). Heyer et al. (2009) emphasized the importance of the dependence of the linewidth on column density and showed that the data on Galactic molecular clouds are consistent with this scaling with $\alpha_{\rm vir} = 1$. By themselves, the GMCs in Solomon et al. (1987)'s sample do not show clear evidence for the $\bar{N}^{1/2}$ scaling; that becomes evident only when higher resolution data are included. Nonetheless, normalizing the Heyer et al. (2009) relation so that it agrees with the linewidth-size relation of Solomon et al. (1987) at the mean column density of the latter's sample ($\bar{N} = 1.5 \times 10^{22}$ cm^{-2}) gives a linewidth-size relation

$$\sigma(r) = 0.72 \left(\frac{\bar{N}_{22}}{1.5}\right)^{1/2} \left(\frac{r}{\rm pc}\right)^{1/2} \ {\rm km\ s^{-1}}\,, \tag{18}$$

We adopt this relation for the 1D velocity dispersion here. The corresponding 3D Mach number is $\mathcal{M} = \sqrt{3}\sigma(r)/c_s$, where the isothermal sound speed is $c_{\rm s}(r) = [x_t kT/(\mu_{\rm H})]^{1/2}$.

At each A_V step we use a precalculated lookup table to find the appropriate two-phase thermal pressure $P_{\rm th}^{\rm 2p} = (P_{\rm max}P_{\rm min})^{1/2}$, as a function of total column density N from the cloud surface and molecular fraction $f({\rm H_2}) = 2N_{\rm H_2}/N$ (see Fig. 2). The pressure is calculated in a manner similar to Wolfire et al. (2003) except that here we include the H_2 self-shielding to depth A_V. The maximum, $P_{\rm max}$, and minimum, $P_{\rm min}$, thermal pressures for a two-phase medium are found from phase diagrams of thermal pressure versus density. In the regime where two-phase pressure dominates, the gas temperature and local density $n_c(r)$ are found self-consistently by iteration. In addition, however, we need the mass-weighted median density in the turbulent medium, $\langle n\rangle_{\rm med}$ (eq. 14), which is a function of the cloud temperature $T(r)$ [through $c_{\rm s}(T)$], and the cloud radius [through $\sigma(r)$, $\bar{n}(r)$, and $T(r)$]. The solution requires two sets of iterations. First, we iterate between $\langle n\rangle_{\rm med}$ and T at each A_V grid point to find a self-consistent density. Second, we convert the A_V grid to a radius grid and rerun the temperature, density iteration.

We note that the H_2 formation rate per unit volume is proportional to $n_{\rm HI}n$, so one might expect that the mass-weighted mean density $\langle n\rangle_{\rm M} = \langle n^2\rangle_{\rm V}/\bar{n} = \bar{n}\exp(2\mu)$ would be appropriate for H_2 formation and thermal balance rather than the median density, $\langle n\rangle_{\rm med} = \bar{n}\exp(\mu)$; here the subscript "V" refers to the volume average. However, in highly supersonic gas, only a very small fraction of the mass is above the mass-weighted mean density, so the bulk of the chemistry occurs in the lower density gas. When the transition from atomic to molecular gas is sharp, then the conditions for the transition are determined by the lower density atomic gas, not by the molecular gas. We also note that numerical simulations of Glover & Mac Low (2007) suggest that H_2 formation proceeds rapidly in a turbulent medium where the H_2 forms in high density gas and remains molecular when transported to

a lower density region. However, using $\langle n \rangle_{\rm M}$ for the typical density at which the formation occurs does not take into account the fact that in very dense regions the gas becomes fully molecular, so that the formation rate drops; thus use of the higher density would overestimate the formation rate. Therefore, we use $\langle n \rangle_{\rm med}$ for the typical density of a clump.

5.1. Results for Clumps in a Turbulent Medium

We have applied our optically thin clump models to molecular cloud masses $M(R_{\rm CO}) = 1{\times}10^5\ M_\odot$, $3{\times}10^5\ M_\odot$, $1{\times}10^6\ M_\odot$, and $3{\times}10^6\ M_\odot$ for incident radiation fields $G_0' = \zeta_{\rm XR}' = 3$, 10, and 30. The lower end of the mass range is chosen to be the lowest cloud mass that could still produce OB stars sufficient to illuminate, heat, and dissociate the molecular cloud with FUV radiation. The upper end is about 1/2 the maximum mass cloud in the Galaxy (Williams & McKee 1997). The range in radiation fields generously covers the expected elevated field from the sum of nearby stellar associations.

We show in Figure 3 (*top*) the calculated thermal pressures for a representative cloud of mass $M(R_{\rm CO}) = 1 \times 10^6\ M_\odot$ with incident radiation fields $G_0' = \zeta_{\rm XR}' = 10$. In this case, the two-phase thermal pressure (i.e., the thermal pressure due to radiative heating) dominates in the outer portion of the cloud, but drops initially due to absorption of EUV/soft X-rays and then due to absorption of FUV by dust. We note that the drop in two-phase pressure is greater than expected from Table 3 in Wolfire et al. (2003). They quote a decrease by a factor ~ 1.8 for $P_{\rm th}^{\rm 2p}$ (given as $P_{\rm ave}$ in that paper) between $N = 10^{19}$ cm^{-2} and $N = 10^{20}$ cm^{-2}, whereas we find a drop by a factor of ~ 3.7. The difference is due to the treatment of cosmic rays: here we do not scale the cosmic ray ionization rate with G_0' but hold it fixed at the local Galactic value. Thus the ionization falls off faster with depth into the cloud than in the Wolfire et al. (2003) models. The turbulent thermal pressure dominates for $A_V \gtrsim 0.001$. The transition to H_2 (at $n_{\rm H_2}/n = 0.25$) occurs at $A_V(R_{\rm H_2}) = 0.34$, the transition to optically thick CO (at $\tau_{\rm CO} = 1$) occurs at $A_V(R_{\rm CO}) = 1.0$, and the dark gas fraction is $f_{\rm DG} = 0.28$.

The calculated densities are shown in Figure 3 (*bottom*). We denote the clump density that would occur in two-phase equilibrium in the absence of turbulence by $n_{\rm 2p}$. For the actual clump density, we take

$$n_c = \max(n_{\rm 2p},\, \langle n \rangle_{\rm med}), \tag{19}$$

where the turbulent mass-weighted median density, $\langle n \rangle_{\rm med}$, is given by equation (14). For the case in the figure, we have $n_c = n_{\rm 2p}$ for $A_V \lesssim 0.001$ and $n_c = \langle n \rangle_{\rm med}$ for $A_V \gtrsim 0.001$. Both H_2 and CO form well within the turbulence-dominated region, a result that holds for

all cloud masses and radiation fields considered here.[3] Note that the volume filling factor $f_{\rm V} \equiv \bar{n}/n_c \sim 0.1$ in the outer part of the cloud where the thermal pressure dominates and two phases exist. Here, WNM fills the rest of the volume with a density of $\sim 10^{-2} n_c$. This implies the mass of the interclump medium is negligible (~ 0.1) compared to the mass in clumps, as we have assumed. In the turbulence-dominated region, there is no such thing as an interclump medium, but rather a distribution of densities that fill the volume. Here, most of the mass is at densities near $\langle n \rangle_{\rm med}$, as assumed.

Figure 4 also shows the temperature distribution (*top*) and the distribution of abundances for C^+, C^0, CO, and OH (*bottom*). The CO amounts to only $\sim 30\%$ of the total carbon abundance when the J=1-0 line becomes optically thick at a CO column density of $N({\rm CO}) \approx 2 \times 10^{16}$ cm^{-2}. Note that we do not include freeze out of H_2O on grains, which would be important at $A_V \gtrsim 3$ (Hollenbach et al. 2009), so our OH chemistry becomes somewhat unreliable at these depths. However, this happens after CO is formed and will not change our results.

For comparison with the $M(R_{\rm CO}) = 1 \times 10^6\ M_\odot$ case we also show in Figures 5 and 6 the results for $M(R_{\rm CO}) = 1 \times 10^5\ M_\odot$. Figure 5 shows the thermal pressures and densities and Figure 6 shows the gas temperature and abundances. The lower cloud mass results in higher $\bar{n}$ (eq. 4) and thus higher clump density (eq. 14) and higher turbulent thermal pressure. The turbulent thermal pressure dominates the two-phase thermal pressure at all A_V. We find $A_V(R_{\rm H_2}) = 0.23$, $A_V(R_{\rm CO}) = 0.95$, and the dark gas fraction $f_{\rm DG} = 0.30$.

The optical depths $A_V(R_{\rm H_2})$ and $A_V(R_{\rm CO})$ are presented in Figure 7 (*top*) for cloud masses $M(R_{\rm CO}) = 1 \times 10^5\ M_\odot$ and $M(R_{\rm CO}) = 3 \times 10^6\ M_\odot$ and for $G_0' = \zeta_{\rm XR}' = 3$, 10, and 30. The optical depths are measured from the cloud surface inward. Figure 7 (*bottom*) shows the cloud radii (measured from the cloud center) corresponding to $A_V(R_{\rm H_2})$, $A_V(R_{\rm CO})$ and the total cloud radius. First, we see that the optical depths to both the H_2 and CO layers increase with increasing radiation fields. (i.e., the transition layers are at greater column densities from the cloud surface). In addition, higher cloud masses result in (slightly) greater optical depths to the transition layers. However, Figure 7 (*top*) shows $\Delta A_{V,\,\rm DG}$ to be nearly constant at $\sim 0.6 - 0.8$ over our entire parameter range.

The cloud radii are shown in Figure 7 (*bottom*). The radius in CO, $R_{\rm CO}$ is fixed from observations by the cloud mass and column density, (eq. 2) and is independent of the incident

[3]We note that the density in the atomic portion of the cloud is close to the value of 230 cm^{-3} given by the theory of Krumholz et al. (2009) for this case ($G_0' = 10,\ Z = 1$). Their result is closely tied to the present work, since they adopt a density of $3n_{\rm min}$, where the expression for the minimum two-phase density, $n_{\rm min}$, is given in Wolfire et al. (2003).

radiation field. The next largest radius, $R_{\rm H_2}$, is also found to be relatively constant with radiation field, reflecting the constancy of $\Delta A_{V,\,\rm DG}$ (Fig. 7, *top*). The largest radius, $R_{\rm tot}$, which encompasses the atomic surface as well as the molecular interior, is found to increase slightly with increasing radiation field, a consequence of the higher column densities required to turn the gas molecular. We also show in Figure 8 the ratio of radii $R_{\rm tot}/R_{\rm CO}$ and $R_{\rm H_2}/R_{\rm CO}$ for cloud masses $M(R_{\rm CO}) = 1 \times 10^5\ M_\odot$ and $M(R_{\rm CO}) = 3 \times 10^6\ M_\odot$.

In Figure 9 we present the calculated dark gas fraction $f_{\rm DG}$ (see eq. 1) for all of the cloud masses and incident radiation fields. We find the fraction is remarkably constant with both cloud mass and radiation field at a value of $f_{\rm DG} \approx 0.3$. As shown in equation (10), the constant fraction follows directly from the constant optical depth between the H_2 and CO layers, and the constant Z' and $\bar{N}$ (or $\bar{A}_V$) assumed in this case.

5.2. Interpretation of Results

The trends in $A_V(R_{\rm H_2})$, $A_V(R_{\rm CO})$, $\Delta A_{V,\,\rm DG}$, and $f_{\rm DG}$ can be understood from the formation/destruction processes for H_2 and CO (Appendices B and C) and the relation between $f_{\rm DG}$ and $\Delta A_{V,\,\rm DG}$ (eq. 10). In Appendix B, we provide an analytic treatment of $A_V(R_{\rm H_2})$ by balancing the formation of H_2 on grains with FUV photodissociation of H_2. There we assume that the density is uniform, and since most of the mass of the cloud is in the clumps or, in the turbulent gas, at density $\langle n \rangle_{\rm med}$, we use the density n_c. Strictly speaking, this density varies somewhat from R_{tot} to $R_{\rm H_2}$, but since the solution heavily depends on what happens at $R_{\rm H_2}$, we use the value of n_c there. The dependence on metallicity, $Z' \equiv Z/Z_\odot$, FUV field and density n_c is given by equation (B9):

$$A_V(R_{\rm H_2}) \simeq 0.142 \ln \left[5.2 \times 10^3 Z' \left(\frac{G_0'}{Z' n_c} \right)^{1.75} + 1 \right]. \tag{20}$$

Here, n_c is in units of $\rm cm^{-3}$. We find that the column density to the transition region is a function of G_0'/n_c consistent with previous investigations (e.g., Sternberg 1988; Hollenbach & Tielens 1999; Wolfire et al. 2008; Krumholz et al. 2008; McKee & Krumholz 2010).

In Appendix C we provide an analytic treatment of $A_V(R_{\rm CO})$ by balancing the formation of CO by gas phase chemistry with FUV photodissociation of CO. The dependence on G_0', n_c, and Z' is given by equation (C7):

$$A_V(R_{\rm CO}) \simeq 0.102 \ln \left[3.3 \times 10^7 \left(\frac{G_0'}{Z' n_c} \right)^2 + 1 \right], \tag{21}$$

where we have substituted the numerical values for the constants into the equation and used $T \sim 50$ K from Figure 4. Taking the difference of equations (21) and (20) we find:

$$\Delta A_{V,\,\mathrm{DG}} = 0.53 - 0.045 \ln\left(\frac{G_0'}{n_c}\right) - 0.097 \ln\left(Z'\right), \tag{22}$$

which leads to

$$\Delta A_{V,\,\mathrm{DG}} = 0.53 - 0.045 \ln\left(\frac{G_0'}{n_c}\right) \tag{23}$$

for $Z' = 1$. Here we have assumed $G_0'/n_c > 0.0075 Z'^{0.43}$ cm^3, as is usually the case, so that one can ignore the factor of unity term inside the brackets of equations (20) and (21). As noted in Appendices B and C, the analytic solutions for $A_V(\mathrm{H_2})$ and $A_V(\mathrm{CO})$ (for $Z' = 1$) agree with the numerical solutions to within 5% and 15% respectively. The analytic solution for $\Delta A_{V,\,\mathrm{DG}}$ (for $Z' = 1$) agrees to within 25% of the model results (Fig. 7).

The principal conclusion of this analysis is that $\Delta A_{V,\,\mathrm{DG}}$ is almost constant (eq. 23), consistent with our numerical results in Figure 7. Equation (10) shows that the dark-gas fraction, f_{DG}, is a function of only $\Delta A_{V,\,\mathrm{DG}}$, which is nearly constant, and of $Z'\bar{N}$ or $\bar{A}_V$. For conditions typical of the Galaxy—$\Delta A_{V,\,\mathrm{DG}} = 0.6 - 0.8$ (Fig. 7), $Z' = 1$ and $\bar{N} = 1.5 \times 10^{22}$ cm^{-2}(or $\bar{A}_V \simeq 8$)—we find $f_{\mathrm{DG}} = 0.26 - 0.33$, in good agreement with the numerical results portrayed in Figure 9. We now discuss the reasons behind these results.

5.2.1. Insensitivity to CO Cloud Mass, $M(R_{\mathrm{CO}})$

Why is f_{DG} so insensitive to the cloud mass? From equation (14), in the limit of large Mach number, the median density goes as $\langle n \rangle_{\mathrm{med}} \propto \bar{n}\mathcal{M} \propto \bar{n}\sigma$. A higher cloud mass results in a lower value of $\bar{n} \propto 1/M(R_{\mathrm{CO}})^{1/2}$ (eq. 4 with $\bar{N}_{22}$ constant), while the turbulent velocity scales as $M(R_{\mathrm{CO}})^{1/4}$. Thus $\langle n \rangle_{\mathrm{med}} \propto 1/M(R_{\mathrm{CO}})^{1/4}$ varies only weakly with cloud mass, with lower densities leading to deeper dissociation layers as the cloud mass increases. However, as seen in equation (23), small changes in n_c lead to very small changes in $\Delta A_{V,\,\mathrm{DG}}$, and thus to very small changes in f_{DG} (see eq. 10).

5.2.2. Insensitivity to Ambient Radiation Field, G_0'

The dark gas fraction is also quite insensitive to variation in the incident radiation field at constant cloud mass, $M(R_{\mathrm{CO}})$. For constant $M(R_{\mathrm{CO}})$, the CO radius, R_{CO}, and the distribution and value of $\bar{n}(r)$ are unchanged, although the total cloud radius increases at the higher radiation fields, and thus $\bar{n}(r)$ drops to lower values in the outer edges of the

cloud. Since $\Delta A_{V,\,\rm DG}$ is also relatively constant with changing G_0', the H_2 radius, R_{H_2}, is unchanged. Since the radii R_{H_2} and $R_{\rm CO}$ are unchanged and the density distribution, $\bar{n}(r)$, is unchanged, we find constant masses and mass fractions. Alternatively, and perhaps more simply, equation (23) shows that $\Delta A_{V,\,\rm DG}$ is very weakly dependent on G_0', and therefore $f_{\rm DG}$ is also weakly dependent as long as $\bar{A}_V$ remains fixed (eq. 10). We note that the ratio of dark-gas mass to *total* mass (including the H I) does decrease with G_0' as we add more shielding H I material to maintain constant $M(R_{\rm CO})$.

We have also investigated the effect of lowering the incident FUV and EUV/soft X-ray fields to $G_0' = \zeta_{\rm XR}' = 1$ for the $M(R_{\rm CO}) = 1 \times 10^6\ M_\odot$ model. We find the dark gas fraction drops slightly from $f_{\rm DG} = 0.28$ to 0.22. The H_2 self-shielding becomes quite strong and draws the H_2 transition close to the surface, resulting in $A_V(H_2) \sim 0.02$, while $A_V({\rm CO})$ is ~ 0.5. Nevertheless, the fitted functions (eqs. 20 and 21) behave quite well and reproduce the model results to within 3% and 8% respectively.

Decreasing the incident field to $G_0' = 0.5$, appropriate for an opaque cloud embedded in the ISRF, further decreases $f_{\rm DG}$ to 0.18. We can check that we are getting reasonable results in the $G_0' = 0.5$ case by comparing with observations of $N_{\rm CO}$ versus A_V. For CO dark clouds, Federman et al. (1990) shows CO column densities of $N_{\rm CO} = 4 \times 10^{16}$ cm^{-2} (twice our fiducial $\tau_{\rm CO} = 1$ surface) at total cloud columns of $A_V \sim 1$, and thus $A_V \sim 0.5$ to the CO emitting gas. This is reasonably consistent with our $G_0' = 0.5$ model that finds $A_V(R_{\rm CO}) = 0.4$. For H_2 we note that steady state PDR models of diffuse gas (Wolfire et al. 2008) find good fits to the observed molecular fractions deduced from UV absorption line studies. The densities ($n \sim 30$ cm^{-3}) in diffuse gas are lower than considered here. However, applying our fitted formula for $A_V(R_{H_2})$ to $G_0' = 0.5$, and $n = 30$ cm^{-3}, yields $A_V(R_{H_2}) \sim 0.23$. This is in good agreement with the transition to high molecular fractions $f(H_2) > 0.1$ found in the diffuse ISM at $A_V \sim 0.26$ (Gillmon & Shull 2006).

5.2.3. Dependence on Cloud Column Density, $\bar{N}$

Equation (10) shows that the dark-gas fraction is sensitive to the mean column density of the cloud. Heyer et al. (2009) have argued that for Galactic molecular clouds, the mean column density within $R_{\rm CO}$ is about half the value we adopted from Solomon et al. (1987), or $\bar{N}_{22} = 1.5/2 = 0.75$. As Heyer et al. (2009) point out, this value is quite approximate, since it depends on an uncertain correction for non-LTE effects in the excitation of ^{13}CO. Bolatto has found the same values for the mean column density ($\bar{N}_{22} = 0.75$) and turbulent velocity in the SMC as Heyer adopts for the Galactic clouds.

To investigate the effects of variations in the mean column density, we have also run $\bar{N}_{22} = 0.75$ models, including the $\bar{N}^{1/2}$ scaling for $\sigma(r)$ suggested by Heyer et al. (2009) (eq. 18). Figure 10 (*bottom*) shows the low column density ($\bar{N}_{22} = 0.75$) results for $M(R_{\rm CO}) = 1 \times 10^6\ M_\odot$ and $Z' = 0.5$, 1, and 1.9. We find higher dark-gas fractions in the $\bar{N}_{22} = 0.75$ models compared to the $\bar{N}_{22} = 1.5$ models; in particular, for $Z' = 1$, $\bar{N}_{22} = 0.75$, and $G'_0 = 10$, the dark-gas fraction $f_{\rm DG} \sim 0.5$, or $M(R_{\rm H_2})/M(R_{\rm CO}) \sim 2$. The change in $f_{\rm DG}$ is almost entirely due to the change in mean column density; the change in $\sigma(r)$ accounts for only a few percent of the increase. There is currently no evidence for such high values of dark-gas mass in the local Galaxy for the high mass clouds that we model here and we favor the higher, $\bar{N}_{22} = 1.5$, value. We note that Grenier et al. (2005) finds higher dark mass fractions in local clouds with very low masses [$M(R_{\rm CO}) < 3 \times 10^4\ M_\odot$]. However, these clouds when observed with high spatial resolution CO observations reveal quite small mean column densities, $\bar{N}_{22} \lesssim 0.2$ (Mizuno et al. 2001; Yamamoto et al. 2006) where we expect the dark gas fraction to be higher than $f_{\rm DG} \sim 0.3$.

5.2.4. Dependence on Metallicity, Z'

In Appendices B and C we explicitly give the dependence of the H_2 and CO formation rates on the metallicity relative to solar, Z'. For H_2, the metallicity enters due to the conversion from A_V to column density, N, and also in the rate of formation of H_2, which proceeds on grain surfaces. For CO, the metallicity enters in the A_V to N conversion and also in the production of OH, which proceeds both on grains and in gas-phase chemical reactions that depend on the gas-phase abundances of oxygen and carbon.

We ran models for our standard cloud mass, $M(R_{\rm CO}) = 1 \times 10^6\ M_\odot$, incident radiation fields $G'_0 = 3$,10, and 30, and for metal abundances $Z' = 0.5$, 1, and 1.9. The $Z' = 0.5$ case is appropriate for molecular clouds in the Large Magellanic Clouds (LMC; Dufour 1984); the $Z' = 1.9$ case is appropriate for clouds in the Galactic Molecular Ring at a Galactocentric radius of 4.5 kpc (Rathborne et al. 2009), based on an exponential scale length for the metallicity in the Galaxy of $H_R^Z = 6.2$ kpc (Wolfire et al. 2003). Figure 10 (*top*) shows that $f_{\rm DG}$ increases with lower metallicity, as predicted by equation (10). In general, the extinction $\Delta A_{V,\,\rm DG}$ between $R_{\rm H_2}$ and $R_{\rm CO}$ is very weakly dependent on Z' (see eq. 22); however, the column density of the dark gas region goes roughly as Z'^{-1} so that the mass in the dark gas increases with lower metallicity.

There is some indication that the dust abundance in low metallicity systems such as the LMC scales as Z'^2 rather than linearly with the metallicity Z' (e.g., Weingartner & Draine 2001). To test the effects of this scaling we ran a model with $Z' = 0.5$ for gas phase metals and

and a dust abundance $Z'^2 = 0.25$. We find $f_{\rm DG}$ increases to $f_{\rm DG} \sim 0.60$, a value intermediate between a $Z' = 0.25$ and $Z' = 0.5$ scaling for both dust and gas phase metals (see Fig. 10). As expected a decrease in the dust abundance at fixed $\bar{N}$ decreases $\bar{A}_V = 5.26 Z' \bar{N}_{22}$ leading to higher dark gas fractions; however, the increase is limited due to the metal dependence of $A_V(R_{\rm CO})$ which leads to smaller $A_V(R_{\rm CO})$ (and thus smaller $\Delta A_{V,\,\rm DG}$) at $Z' = 0.5$ than at $Z' = 0.25$.

We caution against extrapolating our results for varying Z' to very low values of Z'. For fixed $\bar{N}$ and fixed G_0', lowering Z' reduces the size of the molecular interior until first, the entire cloud becomes optically thin in the CO $J = 1 - 0$ transition, and finally, the entire cloud becomes atomic H and C^+. We shall examine the dark-gas fraction for $Z' \ll 0.5$ clouds in the universe in a subsequent paper.

5.2.5. Dependence on Visual Extinction Through the Cloud, $\bar{A}_V$

Equation (10) shows that $f_{\rm DG}$ depends only on $\Delta A_{V,\,\rm DG}/\bar{A}_V$, where $\bar{A}_V \equiv 5.26 Z' \bar{N}_{22}$ is the mean visual extinction through the cloud. As discussed above, $\Delta A_{V,\,\rm DG}$ is only weakly dependent on Z', $\bar{N}_{22}$, G_0 and n_c. Therefore, the main parameter that controls the dark gas fraction is the visual extinction through the cloud, $\bar{A}_V$. Figure 11 clearly shows this dependence; it plots $f_{\rm DG}$ against $\bar{A}_V$ for two different values of Z'= 0.5 and 1.9, holding G_0' fixed at 10 and adjusting the gas density (see eqs. 4, 14, 15, and 18) as $\bar{N}$ changes. Although, at fixed $\bar{A}_V$, the $Z' = 0.5$ case does have a slightly higher value of $f_{\rm DG}$ than the $Z' = 1.9$ case[4], the main parameter controlling $f_{\rm DG}$ is $\bar{A}_V$. If we fix $\bar{N}$, lowering Z' lowers the $\bar{A}_V$ through the cloud, and this is the cause of the large change in $f_{\rm DG}$ seen in Figure 10. Essentially, lowering $\bar{A}_V$ raises the mass of the dark gas located in the surface region *relative to the mass of the interior CO gas, which is fixed in our model*. For $\bar{A}_V = 2$, there is considerable shielded H_2 gas out to large radius around the fixed mass CO "core". For $\bar{A}_V = 30$, the CO "core" takes up much of the cloud, and the dark gas is but a thin shell on the surface.

We have fixed the mass in the CO region in our models because that is what is generally observed. However, to better understand the dependence of $f_{\rm DG}$ on $\bar{A}_V$, it is easier to consider the alternate case of a cloud of fixed *total* mass (i.e., H I + H_2 + CO mass) and variable Z'. As Z' is lowered, the $\bar{A}_V$ through the cloud is lowered. The radius of the CO region, $R_{\rm CO}$,

[4]This slight change is caused by the slight dependence of $\Delta A_{V,\,\rm DG}$ on Z' seen in equation 22 and also because the different Z' cases have different $\bar{N}$, which then means that the gas densities change in the two cases.

shrinks because of the reduced shielding in the cloud. The mass of the CO region drops, as $R_{\rm CO}^2$ since we have assumed that $\bar{n} \propto r^{-1}$. However, the $\Delta A_{V,\,\rm DG}$ is relatively constant through the dark gas shell around the CO, so the column through the shell rises as Z'^{-1}. The mass in the H_2 dark gas, $M(R_{\rm H_2}) - M(R_{\rm CO})$, changes as $R_{\rm eff}^2$ times the column in the shell, where $R_{\rm CO} < R_{\rm eff} < R_{\rm H_2}$. Taking $R_{\rm eff} = R_{\rm CO}$ to obtain the minimum mass in the dark gas, we see that the ratio of dark gas mass to mass in the CO region goes as Z'^{-1} in this case. Therefore, $f_{\rm DG}$ increases as $\bar{A}_V$ decreases (Z' decreases) in this example.

5.2.6. Variation with Cosmic-Rays

The discussion of H_2 and CO in the Appendices is based on the assumption that cosmic-ray ionization is not essential in determining the abundances of these molecules. In order to test the effects of higher cosmic-ray ionization rates, we start with our $G_0' = 10$, $M(R_{\rm CO}) = 1 \times 10^6\ M_\odot$ model, and enhance the cosmic-ray ionization rate by a factor of 10 from low columns to $A_V = 2$ and then drop it back to our standard value so as not to overheat the cloud interior. The enhanced rate tends to increase the production of He^+ from cosmic-ray ionization and increase the destruction of CO through reactions with He^+. The result is to drive the CO slightly deeper into the cloud, but to leave the H_2 surface at the same depth, thereby slightly increasing the dark mass fraction. We find that $f_{\rm DG}$ increases from ~ 0.28 to ~ 0.39.

5.3. Comparison With Observations

First, we note that the dark gas fraction $f_{\rm DG} = 0.28$ for our standard model is in good agreement with the observations of (Grenier et al. 2005), who found $f_{\rm DG} \approx 0.3$. for the four local clouds in their sample that are more massive than $M(R_{\rm CO}) > 3 \times 10^4\ M_\odot$. [5] We note that there is considerable scatter in their dark mass fraction for these 4 clouds, which may indicate scatter in the average extinctions through the clouds, but that the average value of the dark mass fraction is close to our theoretical prediction. In addition, Abdo et al. (2010)

[5]Here we refer to the mass within the CO emitting regions that Grenier et al. (2005) has designated $M_{\rm H_2}$. For clouds more massive than $M(R_{\rm CO}) > 3\times10^4\ M_\odot$ they found dark mass fractions, $f_{\rm DG}$, approximately 0.1 for Cepheus-Cassiopeia-Polaris, 0.1 for Orion, 0.6 for Aquila-Ophiuchus-Libra, and 0.3 for Taurus-Perseus-Triangulum. For lower mass clouds they found 0.5 for Chamaeleon, 0.8 for Aquila-Sagittarius, and 0.6 for Pegasus. The dark gas fractions for high mass clouds found by Abdo et al. (2010) are 0.30 for Cepheus, and 0.37 for Cassiopeia, and 0.36 for the low mass Polaris cloud.

from observations of nearby resolved clouds find an average value of $f_{\rm DG} \approx 0.34$ for their two massive clouds. Grenier et al. (2005) and Abdo et al. (2010) find $f_{\rm DG}$ higher than 0.3 in very low mass clouds [$M(R_{\rm CO}) < 3 \times 10^4\ M_\odot$] where the mean extinction is observed to be much less than our standard value and a higher $f_{\rm DG}$ is consistent with our prediction.

Next, we compare our numerical results with the observations of H I halos around molecular clouds in the Galaxy. Wannier et al. (1983) observed H I halos around 8 molecular clouds and concluded they extend several parsecs beyond the CO and have a thickness of a few parsecs. In addition, the halos are "warm," having temperatures of at least $50 - 200$ K in order to be seen in emission over the background. We note that the use of "warm" in their title has been interpreted by others to mean gas at temperatures of ~ 8000 K, but in fact they cite temperatures of order a few 100 K.

Andersson et al. (1991) and Andersson & Wannier (1993) included additional data and analysis and report H I integrated intensities between 700 K km s^{-1} and 4300 K km s^{-1} and characteristic depths of about 4.7 pc. Based on model fits, they estimate H I densities $n_{\rm HI} \sim 25 - 125$ cm^{-3} and temperatures $T \sim 50 - 200$ K. We note that they suggested that either the formation rate of H_2 was lower than the standard rate or the FUV field was about 10 times the interstellar value in order to simultaneously match the CO and H I observations. At that time they favored the lower H_2 formation rate since an increased FUV field would produce too little OH compared to observation. However subsequent, work by Hollenbach et al. (2009) showed that OH is formed at greater abundances than previously thought when grain surface chemistry is included. Thus, their suggestion that the FUV field is enhanced near GMCs is consistent with a similar result by Wolfire, Hollenbach, & McKee (2010, in preparation) in modeling the average FUV field illuminating a star-forming molecular cloud.

For cloud masses in the range $M(R_{\rm CO}) = (1 - 10) \times 10^5\ M_\odot$ and for $G_0' = 10 - 30$, we find H I integrated intensities from 965 K km s^{-1} to 4100 K km s^{-1} and a range in H I halo thickness from 1 pc to 10 pc. These are in good agreement with the observations. At $A_V(R_{\rm H_2})$, our temperature range $T = 70 - 80$ K and density range $\bar{n} = 45 - 147$ cm^{-3} agree with that of Andersson & Wannier (1993). Therefore, we consider the model to be in very good agreement with these observations.

We note that CO-to-H_2 conversion factors have been inferred from gamma-ray and far-infrared observations, and also from virial mass estimates. The gamma-ray (Strong & Mattox 1996) and far-infrared (Dame et al. 2001) estimates include the "dark gas" and are $X = 1.9 \times 10^{20}$ cm^{-2} (K km s^{-1})$^{-1}$ and $X = 1.8 \times 10^{20}$ (K km s^{-1})$^{-1}$ from gamma-ray observations and far-infrared observations respectively. However, these values are Galactic averages and observations of nearby resolved clouds show a variable X increasing towards the outer

Galaxy (Abdo et al. 2010). The Abdo et al. observations separate the "dark gas" and CO components and generally show lower X ratios [$X \sim 0.87 \pm 0.05 \times 10^{20}$ cm^{-2} (K km s^{-1})$^{-1}$]. Depending on whether the dark gas is mixed with other components the X value could be lower if mixed with H I or raised if mixed with CO. The Solomon et al. (1987) conversion factor was based on a virial cloud estimate and for an idealized cloud would not include the "dark gas". McKee & Ostriker (2007) re-evaluated their conversion, accounting for an 8.5 kpc distance to the Galactic center and including the He mass, and found a revised Solomon et al. value of $X = 1.9 \times 10^{20}$ cm^{-2} (K km s^{-1})$^{-1}$. In general, the X ratios derived from virial mass estimates exceed those based on gamma-ray observations from resolved clouds by factors of 1.5-3.0 (Abdo et al. 2010). However, turbulent mixing of the bright CO and dark gas could easily cause the virial estimate to include some of the dark gas. Therefore, one should note that CO to H_2 conversion factors are sometimes normalized to implicitly include the dark mass, even though it lies outside the CO gas.

5.4. Justification of the Optically Thin Approximation

One of the important approximations in our work is that the density fluctuations in the molecular cloud—the clumps—are optically thin, or $A_V < 1$ through each clump. This approximation can now be justified in light of our results: the fact that the dark-gas fraction depends primarily on $\bar{A}_V$, the mean visual extinction through the entire cloud, but only weakly on the density and radiation field, implies that it is insensitive to the distribution of matter within the cloud. Consider an extreme example of a cloud with very opaque clumps, namely a cloud with clumps so opaque that their mean extinction is equal to that of the entire cloud, $\bar{A}_V \sim 8$. We assume that the cloud with opaque clumps has the same mean $\bar{A}_V$, and clump density, n_c, as the cloud with transparent clumps. For simplicity we assume that there is no radial variation in the properties of the clumps. Let a be the clump radius. Then the number of clumps, $\mathcal{N}$, is determined by the condition that the clumps occupy a fraction $f_{\rm V}$ of the volume:

$$\mathcal{N} a^3 = f_{\rm V} R_{\rm tot}^3. \tag{24}$$

The condition that the clumps have the same $\bar{A}_V$ as the cloud as a whole gives

$$n_c a = \bar{n} R_{\rm tot} = f_{\rm V} n_c R_{\rm tot}, \tag{25}$$

so that $a = f_{\rm V} R_{\rm tot}$. When viewed from the outside, the fraction of the cloud that is covered by clumps (the projected covering factor) is then

$$C = \frac{\mathcal{N} \pi a^2}{\pi R_{\rm tot}^2} = 1, \tag{26}$$

as expected. From the perspective of a clump inside the cloud, this means that about half the sky is covered by clumps, since, on average, the path length from a clump to the surface of the cloud is half the path length through the entire cloud. The average radiation field incident on a clump is therefore reduced by about a factor 2 compared to the radiation field incident on the cloud as a whole.

We can now estimate the dark-gas fraction of a cloud of these opaque clumps. Each clump will have a dark-gas fraction that is almost the same as that of the entire cloud, modified only by the reduction in G_0' by about a factor of 2. Since the extinction of the dark gas layer depends only weakly on the intensity of the radiation field, $\Delta A_{V,\,\rm DG} \propto 0.045 \ln G_0'$, this modification is very slight for typical values of $\bar{A}_V \sim 8$ (see eq. 10). This argument does not prove that clumps with $\bar{A}_V$ intermediate between the large value ~ 8 assumed here and the small values $\bar{A}_V < 1$ assumed in the rest of this work will also have the same dark-gas fraction. However, because this range $1 < \bar{A}_V < 8$ is small it strongly suggests that this is the case. We conclude that inclusion of finite optical depth of clumps in a cloud is unlikely to significantly alter our conclusions.

5.5. Justification of Assumption of Steady State Chemistry

Our models solve for the steady state abundances of the atomic and molecular species. In this subsection we examine the assumption of steady state chemistry in the turbulent molecular cloud surfaces by comparing the chemical and dynamical times at the cloud depth $A(R_{\rm H_2})$. The chemical timescale, $t_{\rm chem}$, is the time for atomic gas to become completely molecular ($n_{\rm H_2} = 0.5\langle n \rangle_{\rm med}$), thus $t_{\rm chem} = 0.5/(\mathcal{R}\langle n \rangle_{\rm med})$ where $\mathcal{R} = 3 \times 10^{-17} Z'$ cm^3 s^{-1} is the rate coefficient for H_2 formation on dust grains (see Appendix B). To compute the dynamical timescale, $t_{\rm dyn}$, we require the characteristic distance for the turbulence to bring molecular gas from the interior to the surface, and to bring atomic gas from the surface to the interior, where the interior is A_V greater than $A_V(R_{\rm H_2})$. This characteristic distance is $d_{\rm dyn} = 1.9 \times 10^{21} A_V(R_{\rm H_2})/\bar{n}$. The dynamical timescale is this distance divided by the turbulent velocity for lengthscale $d_{\rm dyn}$, $t_{\rm dyn} = d_{\rm dyn}/\sigma(d_{\rm dyn})$ where σ is the 1D turbulent velocity dispersion (eq. 18).

For a cloud mass $M(R_{\rm CO}) = 10^5\ M_\odot$, and $Z' = 1$, we find $\bar{n} \approx 140$ cm^{-3}, and $\langle n \rangle \approx 600$ cm^{-3} at $A_V(R_{\rm H_2}) = 0.22$ and thus $t_{\rm chem} \sim 2.8 \times 10^{13}$ s, $d_{\rm dyn} \sim 1.0$ pc, and $t_{\rm dyn} \sim 4.3 \times 10^{13}$ s. Comparing chemical and dynamical timescales we find $t_{\rm chem}/t_{\rm dyn} = 0.65$. Similarly, for $M(R_{\rm CO}) = 10^6\ M_\odot$ we find $t_{\rm chem}/t_{\rm dyn} = 0.48$. For $t_{\rm chem}/t_{\rm dyn} \lesssim 1$, a steady state approximation is valid since gas has time to reach steady state before significant turbulent mixing. We find ratios less than one, but only marginally so, and thus we expect some affects

from turbulence. We note however that turbulence brings atomic gas inward past $A_V(R_{H_2})$ into the molecular gas, and at the same time it brings molecular gas to the surface. Thus, the first order effect is to spread out the rise of x_{H_2}, but not to move $A_V(R_{H_2})$. In addition, we have demonstrated in subsection (5.3) that the steady state model is in good agreement with observations, and thus the effects of turbulence are modest.

6. Discussion and Summary

6.1. Model Assumptions

We have constructed models of molecular clouds to investigate the fraction of gas that is mainly H_2 and contains little CO. These conditions exists where the CO is photodissociated into C and C^+ but the gas is molecular H_2 due to either H_2 self-shielding or dust shielding. Such conditions can exist either on the surfaces of molecular clouds or the surfaces of clumps contained within such clouds. Observations indicate that the mass in this "dark gas" can be as high as 30% of the total molecular mass in the local Galaxy. Previous theoretical plane-parallel models of individual PDRs have indicated that such a layer should exist (e.g., van Dishoeck & Black 1988), but here we construct models directed towards molecular clouds as a whole while including observational constraints on cloud mass, radius, average density, and line width and theoretical considerations of the likely strengths of the UV fields impinging on GMCs.

We assume that the surface of each cloud is isotropically illuminated over 2π steradians by a soft X-ray/EUV field and an FUV radiation field. We use the standard cosmic-ray ionization rate of 1.8×10^{-17} s^{-1} per hydrogen nucleus everywhere in the cloud for all cases but one test case. There is evidence from observations of H_3^+ that the cosmic-ray ionization rate is a factor of 10 higher in some portions of the diffuse ISM (Indriolo et al. 2007), but there is no indication that such rates apply in molecular cloud interiors (McCall et al. 1999). In preliminary work of M. Wolfire et al. (2010, in preparation) we find that the average FUV field on clouds is ~ 20 times the local Galactic interstellar field. This elevated field arises from the distribution of OB associations around the cloud.

The distribution of temperature, density, and abundances within the H I, H_2, and CO layers are calculated using the PDR code of Kaufman et al. (2006). In constructing model clouds from the PDR output, we impose the constraint from Solomon et al. (1987) that the typical column density through the cloud is $\bar{N}_{22} = 1.5$, independent of cloud mass and independent of radius inside a given cloud (since $\bar{n} \propto r^{-1}$). The locally averaged density $\bar{n}$ and radius of the CO cloud, R_{CO}, as functions of the CO-cloud mass, $M(R_{CO})$ follow from

equations (2) and (4). In our notation, $M(R_{\rm CO})$ is the molecular mass contained within the $\tau_{\rm CO} = 1$ surface (of the CO $J = 1 - 0$ transition) including the mass of H_2 and He, and $R_{\rm CO}$ is the radius of this CO photosphere. We impose a volume-averaged density distribution $\bar{n}(r)$ that behaves as $\bar{n} \propto 1/r$ throughout all layers of the cloud. Note that in regions where the thermal pressure $P_{\rm th}$ lies between $P_{\rm min}$ and $P_{\rm max}$ both warm ($T \gtrsim 7000$ K) and cold ($T \lesssim 500$ K) gas solutions are possible. In this regime we use the cold solution from our model results with n_c the density of the cold clumps and $\bar{n}$ the average over cold and warm gas components. The warm gas fills the volume, but contains little of the mass.

We test two extreme limits for clumps within the cloud, one in which all clumps are optically thin to the incident FUV field, and one in which all clumps are optically thick to the incident FUV field. In the optically thin approximation, the PDR model output as a function of A_V gives directly the distribution in A_V throughout the cloud. In the optically thin limit we test two different models for the cloud density distribution. First we use constant thermal pressure models and second we include two sources of thermal pressure, radiative heating (which by itself would lead to a two-phase equilibrium) and supersonic turbulence. The distribution of two-phase thermal pressure is calculated as in Wolfire et al. (2003) and stored in a look-up table as a function of total column density and molecular fraction (see Fig. 2). This pressure drops as one moves into the cloud due to the absorption of the radiation responsible for heating the gas. Supersonic turbulence is characterized by a mass-weighted median density $\langle n \rangle_{\rm med} = \bar{n} \exp(\mu)$, with $\mu = 0.5 \ln(1+0.25\mathcal{M}^2)$ (Padoan et al. 1997). When the two-phase pressure drops below $P_{\rm th}^{\rm turb} \equiv x_t \langle n \rangle_{\rm med} kT$, where x_t is the sum over the abundances of all species relative to hydrogen nuclei, we assume that the turbulence maintains the gas at a thermal pressure $P_{\rm th}^{\rm turb}$. The sound speed that enters in the Mach number is calculated from the PDR model output while the turbulent velocity is given by the linewidth-size relation (eq. 18).

In the limit of very optically thick clumps (with optical depths at least as large as the average optical depth through the cloud), we find that the average radiation field on a clump ranges between about $G_0'/2$ to G_0'. In this limit, the dark mass fraction of a clump is the same as the dark mass fraction of the entire cloud. Since the dark gas mass fraction of a spherical clump or a spherical cloud is insensitive to the incident FUV field (see eqs. 10 and 22), the dark mass fraction of the cloud does not change significantly compared with the case of a cloud made up of optically thin clumps.

We have tested the steady state assumption for the chemistry by comparing the time to form molecular hydrogen, $t_{\rm chem}$, with the dynamical time, $t_{\rm dyn}$, for turbulence to bring molecular gas from the interior to the surface and to bring atomic gas to the interior. We find $t_{\rm chem}/t_{\rm dyn} \sim 0.7$ for a cloud mass of $M(R_{\rm CO}) = 1 \times 10^5\ M_\odot$ and $t_{\rm chem}/t_{\rm dyn} \sim 0.5$ for a

cloud mass of $M(R_{\rm CO}) = 1 \times 10^6\ M_\odot$. Thus we expect modest affects due to turbulence; mainly to spread out the transition from atomic to molecular hydrogen but not to move $A_V(R_{\rm H_2})$. We also note that steady state models agree well with observations.

6.2. Dark-Gas Fraction

For our standard cloud mass, $M(R_{\rm CO}) = 1 \times 10^6\ M_\odot$, and incident radiation field, $G_0' = \zeta_{\rm XR}' = 10$, we find dark-gas mass fractions of $f_{\rm DG} = 0.28$ and $f_{\rm DG} = 0.31$ for constant thermal pressures of $P_{\rm th} = 10^5$ K cm^{-3} and $P_{\rm th} = 10^6$ K cm^{-3}, respectively. These correspond to a total molecular mass $M(R_{\rm H_2}) \approx 1.4 M(R_{\rm CO})$. For models that include both thermal and turbulent pressures, we find essentially the same results as for the cases with constant thermal pressure. The variation in $f_{\rm DG}$ ranges from 0.25 to 0.33 over a range in G_0' from 3 to 30 and a range in cloud mass from $10^5\ M_\odot$ to $3 \times 10^6\ M_\odot$ (Fig. 9). Figure 3 shows the distribution in thermal pressures and densities and Figure 4 shows the distribution in temperatures and chemical abundances for the standard model.

The constant value of $f_{\rm DG}$ for fixed $\bar{A}_V$ can be understood from the analytic solutions for $A_V(R_{\rm H_2})$ and $A_V(R_{\rm CO})$ in Appendices B and C and the expression for $f_{\rm DG}$ in equation (10). In the limit of $G_0'/n > 0.0075 Z'^{0.43}$ cm^3, both $A_V(R_{\rm H_2})$ and $A_V(R_{\rm CO})$ increase as $\ln(G_0'/n)$. Thus, the optical depth through the H_2 layer $\Delta A_{V,\,\rm DG}$ is a weak function of G_0'/n and Z' (eq. 22) and is nearly constant over our parameter space. Furthermore, we find that $f_{\rm DG}$ is a function of only $\Delta A_{V,\,\rm DG}$ and the mean extinction through the cloud $\bar{A}_V \equiv 5.26 Z' \bar{N}_{22}$ (Eq. 10); thus, for a given $\bar{A}_V$, the dark-gas fraction is constant. However, $f_{\rm DG}$ increases significantly if $\bar{A}_V$ decreases.

Our numerical results compare well with observations of the local Galactic dark-gas fraction, which Grenier et al. (2005) find to be $f_{\rm DG} \sim 0.3$, when averaged over their four most massive clouds with masses between $3 \times 10^4 - 3 \times 10^5$ M$_\odot$. Lower mass clouds observed by Grenier et al. (2005) are observed to have low $\bar{A}_V$ and thus high dark-gas fractions consistent with our prediction. Our H I integrated intensities of 965 K km s^{-1} to 4100 s^{-1} , H I cloud-halo thickness of 1 pc to 10 pc, average cloud densities of $\bar{n} \sim 45 - 150$ cm^{-3}, and average H I temperatures of $\sim 70 - 80$ K are in good agreement with the observations of H I cloud halos observed by Wannier et al. (1983), Andersson et al. (1991), and Andersson & Wannier (1993).

We have carried out several additional tests to assess the dependence of our results on the cosmic-ray ionization rate, the clump optical depth, the mean cloud column density, the metallicity, and the mean visual extinction through the cloud. We ran our standard model

with the cosmic-ray ionization rate a factor of 10 higher at $A_V < 2$, as suggested by H_3^+ observations in some regions of the diffuse ISM, and found that this enhanced cosmic-ray rate only slightly increases the dark-gas fraction. In the limit of very optically thick clumps we find no significant change in $f_{\rm DG}$.

Heyer et al. (2009) has suggested that the mean column density (and therefore the mean visual extinction $\bar{A}_V$) in Galactic CO clouds is about half the value found by Solomon et al. (1987), i.e., $\bar{N}_{22} \simeq 0.75$ or $\bar{A}_V \simeq 4$. The results of changing the mean column density, the metallicity, and the mean visual extinction through the cloud are illustrated in Figures 10 and 11. We find that the dark-gas fraction increases with lower extinction since the dark gas occupies a larger fraction of the cloud (see eq. 10). There is also a weak dependence of $\Delta A_{V,\,\rm DG}$ on the mean column density that tends to slightly mitigate the dominant effect. Lower mean columns lead to lower mean densities (eq. 4) and lower n_c (eqs. 14 and 19), and thus lower $\Delta A_{V,\,\rm DG}$ (eq. 22). We examine metallicities appropriate for the LMC ($Z' = 0.5$), for the local Galaxy ($Z' = 1$), and for the molecular ring at $R = 4.5$ kpc ($Z' = 1.9$). In general, $f_{\rm DG}$ increases as the metallicity drops for fixed columns because the mean extinction through the cloud decreases, which raises the ratio of the surface dark gas to the interior CO gas (again, see eq. 10). There is also a weak dependence of $\Delta A_{V,\,\rm DG}$ on Z' that also slightly increases $\Delta A_{V,\,\rm DG}$ (or $f_{\rm DG}$) with decreasing Z' (eq. 22) even if the column is changed so that $\bar{A}_V$ remains fixed. We note that in the case of varying $\bar{N}$ and Z', but at constant $\bar{N}Z'$ or $\bar{A}_V$ (see Figure 11), the change in $f_{\rm DG}$ is entirely due to the weak dependencies of $\Delta A_{V,\,\rm DG}$ on $\bar{N}$ and Z' as noted above and shown in equation (22). We also examine the case for dust scaling as Z'^2 ($= 0.25$) while gas phase metals scale as Z' ($= 0.5$). We find $f_{\rm DG}$ is larger than when both metals and gas scale together.

In Appendices B and C we derive analytic solutions for $A_V(R_{\rm H_2})$ and $A_V(R_{\rm CO})$ as functions of density n, FUV field G_0', and metallicity Z'. For the case of H_2 we find an expression for the abundance of H_2 by balancing formation and destruction processes and then solving for the position where $n_{\rm H_2} = 0.25n$. Similar studies have been carried out by, for example, Sternberg (1988); McKee & Krumholz (2010). We find our fits are good to $\pm 5\%$ for all models presented in this paper. The fits to CO are found by integrating the expression for the abundance of CO to a column density of $N({\rm CO}) = 2 \times 10^{16}$ cm^{-2}, where $\tau_{\rm CO} = 1$ (the optical depth of the CO J= 1-0 transition). The fits are generally good to within $\pm 15\%$ except for the lowest Z' and G_0' model, where the fit is good to $\pm 25\%$. We have also derived analytic expressions for $\Delta A_{V,\,\rm DG}$ and $f_{\rm DG}$ in the main text (eqs. 22 and 10, respectively).

The overall result of this paper is a theoretical derivation that $f_{\rm DG} \simeq 0.3 \pm 0.08$ for GMCs with $\bar{A}_V \simeq 8$ in our Galaxy. Therefore, a significant fraction of the molecular gas

in our Galaxy lies outside the CO gas. As discussed in §2.4.2, some calibrations of the CO line intensities to H_2 mass take into account this "dark" H_2 gas. However, it is important to be aware of this component since it contributes significantly to the gamma ray, infrared/submillimeter continuum, and [CII] 158 μm emission from clouds in galaxies. Its contribution to the star formation in a galaxy is as yet undetermined. The importance of this component increases as the metallicity decreases, such as in the outer regions of galaxies or in low metallicity galaxies.

Although the gas in the C^+/H_2 layer is termed "dark gas," it emits [C II] 158 μm line emission and the dust in the dark layer emits infrared continuum. In a subsequent paper we will estimate the emission from the "dark gas". In addition, a future paper will model in detail the lower metallicity clouds found, for example, in the SMC and early universe.

Partial support for M.G.W. and D.J.H. was provided by a NASA Long Term Space Astrophysics Grant NNG05G64G. Partial support for D.J.H was also provided by NASA's Stratospheric Terahertz Observatory project, grant NNX08AG39G. Support for CFM was provided in part by the National Science Foundation through grant AST-0908553. We thank Alberto Bolatto and Eve Ostriker for useful discussions. We also thank an anonymous referee for a careful reading of this manuscript and for several very helpful comments.

A. Dark-Gas Mass Fraction

Here we determine the dark-gas mass fraction,

$$f_{\rm DG} \equiv \frac{M(R_{\rm H_2}) - M(R_{\rm CO})}{M(R_{\rm H_2})} \ , \tag{A1}$$

for clouds with a power-law gradient for the mean density,

$$\bar{n} = \bar{n}(R_{\rm H_2}) \left(\frac{R_{\rm H_2}}{r} \right)^{k_\rho} , \tag{A2}$$

for $k_\rho < 3$ (the reason for normalizing the density at $R_{\rm H_2}$ will become apparent below). GMCs typically have $k_\rho \simeq 1$ (Larson 1981), which is the case considered in the text. For $k_\rho < 3$, the mass inside a radius r is

$$M(r) = \frac{4\pi \bar{n}(R_{\rm H_2}) \mu_{\rm H} R_{\rm H_2}^{k_\rho}}{3 - k_\rho} \ r^{3-k_\rho}, \tag{A3}$$

and the mean column density inside r is

$$\bar{N}(R_{\rm H_2}) \equiv \frac{M(R_{\rm H_2})}{\mu_{\rm H} \pi R_{\rm H_2}^2} = \frac{4 R_{\rm H_2} \bar{n}(R_{\rm H_2})}{3 - k_\rho} \ , \tag{A4}$$

where $\mu_{\rm H}$ is the mean mass per H nucleus. For $k_\rho \neq 1$, the column density of the dark-gas layer is

$$\Delta N_{\rm DG} = \bar{n}(R_{\rm H_2}) \int_{R_{\rm CO}}^{R_{\rm H_2}} \left(\frac{R_{\rm H_2}}{r'}\right)^{k_\rho} dr', \tag{A5}$$

$$= \bar{N}(R_{\rm H_2}) \left(\frac{3-k_\rho}{k_\rho - 1}\right) \left[\left(\frac{R_{\rm H_2}}{R_{\rm CO}}\right)^{k_\rho - 1} - 1\right], \tag{A6}$$

where we used equation (A4) in the second step. The mass fraction of the dark gas (eq. A1) becomes

$$f_{\rm DG} = 1 - \left(\frac{R_{\rm CO}}{R_{\rm H_2}}\right)^{3-k_\rho} \tag{A7}$$

with the aid of equation (A3). Equation (A6) then implies

$$f_{\rm DG} = 1 - \left[1 + 4\left(\frac{k_\rho - 1}{3-k_\rho}\right) \frac{\Delta N_{\rm DG}}{\bar{N}(R_{\rm H_2})}\right]^{-(3-k_\rho)/(k_\rho - 1)}, \tag{A8}$$

$$= 1 - \left[1 + \left(\frac{k_\rho - 1}{3-k_\rho}\right) \frac{0.76 \Delta A_{V,\,\rm DG}}{Z' \bar{N}_{22}(R_{\rm H_2})}\right]^{-(3-k_\rho)/(k_\rho - 1)}, \tag{A9}$$

where we used equation (3) in the second step. Taking the limit as $k_\rho \to 1$ gives equation (8) in the text, since $\Delta N_{\rm DG} = N_0 \Delta A_{V,\,\rm DG}$ and $\bar{N}$ is constant, so the argument $R_{\rm H_2}$ is not needed.

In order to see how the dark-gas fraction depends on the density gradient, we rewrite equation (A9) as

$$f_{\rm DG} = 1 - \left(1 + \frac{x}{\alpha}\right)^{-\alpha}, \tag{A10}$$

with

$$x \equiv \frac{4\Delta N_{\rm DG}}{\bar{N}(R_{\rm H_2})} = \frac{0.76 \Delta A_{V,\,\rm DG}}{Z' \bar{N}_{22}(R_{\rm H_2})}, \tag{A11}$$

$$\alpha \equiv \frac{3-k_\rho}{k_\rho - 1}. \tag{A12}$$

If the dark gas corresponds to a relatively small fraction of the total extinction ($x \ll 1$), then

$$f_{\rm DG}(k_\rho) - f_{\rm DG}(k_\rho = 1) \simeq \frac{x^2}{2\alpha}. \tag{A13}$$

For $0 \leq k_\rho \leq \frac{3}{2}$, where $|\alpha| \geq 3$, the magnitude of the difference between the actual dark-gas fraction and that found in the text, where k_ρ is taken to be unity, is $\leq x^2/6$. This is typically small: For $\Delta A_{V,\,\rm DG} < 1$ and $Z' \bar{N}_{22} \simeq 1.5$, as in the text, we have $x < 0.5$ and $|f_{\rm DG}(k_\rho) - f_{\rm DG}(k_\rho = 1)| < 0.04$. For the case $\bar{N}(R_{\rm H_2}) \ll 4\Delta N_{\rm DG}$ ($x \gg 1$) we see from equation (A10) that $f_{\rm DG} \sim 1$.

B. Analytic Treatment of $A_V(H_2)$

The analytic treatment of the H/H_2 transition assumes that H_2 is formed on interstellar dust grains with an effective formation rate coefficient of $\mathcal{R} = 3 \times 10^{-17}$ cm^3 s^{-1}, and is destroyed by FUV photodissociation with an unshielded rate of $I_0 = 6 \times 10^{-11}$ s^{-1} in the Habing (1968) field (1.6×10^{-3} erg cm^{-2} s^{-1}) or $I_0' = 1.02 \times 10^{-10}$ s^{-1} in the Draine (1978) field, which is 1.7 times stronger. In order to simulate an isotropic field incident from 2π steradians on an optically thick slab, we assume a 1D FUV flux incident at an angle of 60 degrees with the normal to the slab. Consequently, to penetrate to a (normal) distance x into the slab, a photon needs to travel $2x$. In a steady state in which the photodissociation of molecular hydrogen is balanced by the formation on dust grains, we have

$$G_0' I_0' f_s n_{H_2} e^{-2 b_{H_2} A_V} = \mathcal{R} Z' n n_{HI}, \tag{B1}$$

where G_0' is the energy density of the dissociating radiation field in units of the Draine (1978) field, f_s is the H_2 self-shielding factor (see below), n_{H_2} is the number density of molecular hydrogen, b_{H_2} is the dust attenuation factor that accounts for differences in attenuation between the visible and the FUV and also approximately includes the effects of FUV scattering, A_V is the visual extinction into the slab normal to the surface (see eq. 5), n is the hydrogen nucleus number density, and n_{HI} is the atomic hydrogen number density. In this Appendix and the following one, we are treating the gas in the clumps, where most of the mass resides. Therefore, there is no need to distinguish the density n from the local clump value n_c. The factor of 2 in the exponential follows from the factor of 2 longer pathlength due to the oblique incidence of the FUV flux (see above). We assume that the surface area of grains increases proportionally to the increase in metallicity Z', so that both the H_2 formation rate coefficient and the FUV extinction increase linearly with Z'.

In order to obtain a relatively simple analytic approximation to the variation of n_{H_2} with depth into the slab, we require that the self-shielding factor be approximated by a power law with the form

$$f_s = \left[\frac{N_1}{2 N_{H_2}} \right]^d , \tag{B2}$$

where N_1 is a constant that is determined by comparison with detailed numerical calculations (see below), N_{H_2} is the H_2 column density measured normal to the cloud surface, and the factor 2 is due to the longer pathlength associated with the 60 degree incidence angle.

We wish to find an analytic expression for $A_V(R_{H_2})$, where $A_V(R_{H_2})$ is defined as the characteristic value of the (normal) visual extinction to the point in the slab at which the hydrogen makes the transition from atomic to molecular form. We define this to be at the point where $n_{H_2} = 0.25n$ and $n_{HI} = 0.5n$. In other words, $A_V(R_{H_2})$ is where the hydrogen is

half atomic and half molecular.[6] We denote the corresponding column densities by $N(R_{\rm H_2})$; for example, $N_{\rm H_2}(R_{\rm H_2})$ is the column of H_2 from the surface of the cloud at R_{tot} to $R_{\rm H_2}$, or the column of H_2 to a depth given by $A_V(R_{\rm H_2})$.

Substituting $n_{\rm H_2} = 0.25n$ and $n_{\rm HI} = 0.5n$ into equation (B1) we obtain for the H_2 column $N_{\rm H_2}(R_{\rm H_2})$ corresponding to $A_V(R_{\rm H_2})$

$$N_{\rm H_2}(R_{\rm H_2}) = 0.5 N_1 \left(\frac{G_0' I_0'}{2\mathcal{R} Z' n}\right)^{1/d} e^{-2b_{\rm H_2} A_V(R_{\rm H_2})/d} \; . \tag{B3}$$

We can also multiply equation (B1) by dx and integrate into the slab to obtain an expression for $N_{\rm H_2}$ as a function of N or A_V into the slab. We obtain the general solution up to the point $N_{\rm H_2}(R_{\rm H_2})$ or $A_V(R_{\rm H_2})$ where the gas is half atomic and half molecular. In order to simplify this integration, we assume that $n_{\rm HI} = c_1 n$ and is constant for $N < N_{\rm H_2}(R_{\rm H_2})$. Note that c_1 varies from 1 at small column to 0.5 as we approach $A_V(R_{\rm H_2})$, and it can be adjusted to best match the numerical code results. Since the solution heavily depends on what happens near $A_V(R_{\rm H_2})$, we expect $c_1 \simeq 0.5$; in addition, we expect the density to be $n \simeq n(R_{\rm H_2})$. For $d < 1$ (which we show later is always the case) we obtain:

$$N_{\rm H_2} = 0.5 \left[\frac{(1-d) c_1 \mathcal{R} Z' n N_0}{b_{\rm H_2} G_0' I_0' N_1^d}\right]^{1/(1-d)} \left(e^{2b_{\rm H_2} A_V} - 1\right)^{1/(1-d)} \; . \tag{B4}$$

Substitution of $A_V = A_V(R_{\rm H_2})$ into this equation yields another expression for $N_{\rm H_2}(R_{\rm H_2})$ as a function of $A_V(R_{\rm H_2})$.

Equating the two expressions for $N_{\rm H_2}(R_{\rm H_2})$ (eqs. B3 and B4), we obtain a trancendental equation whose solution gives $A_V(R_{\rm H_2})$:

$$\left[\frac{(1-d) c_1 \mathcal{R} Z' n N_0}{b_{\rm H_2} G_0' I_0' N_1^d}\right]^{1/(1-d)} \left(e^{2b_{\rm H_2} A_V(R_{\rm H_2})} - 1\right)^{1/(1-d)} = N_1 \left(\frac{G_0' I_0'}{2\mathcal{R} Z' n}\right)^{1/d} e^{-2b_{\rm H_2} A_V(R_{\rm H_2})/d} \; . \tag{B5}$$

We can obtain analytic solutions in the two limits of small $A_V(R_{\rm H_2})$ and large $A_V(R_{\rm H_2})$. In the limit $A_V(R_{\rm H_2}) \ll [2b_{\rm H_2}]^{-1} \sim 0.25$ (see below), which corresponds to no appreciable dust extinction of FUV and entirely self-shielding by H_2, we obtain

$$A_V(R_{\rm H_2}) \simeq \frac{1}{(1-d) c_1} \left(\frac{G_0' I_0'}{2\mathcal{R} Z' n}\right)^{1/d} \left(\frac{N_1}{N_0}\right) \; . \tag{B6}$$

[6]Note that the simple power law expression given in equation (B2) need only apply for shielding columns $N_{\rm H_2} \sim 10^{18-20}$ cm^{-2} that correspond to typical H_2 columns at positions in the slab with A_V somewhat less than or equal to $A_V(R_{\rm H_2})$.

In the limit $A_V(R_{H_2}) \gg [2b_{H_2}]^{-1} \sim 0.25$, which corresponds to significant dust extinction as well as self-shielding, we obtain

$$A_V(R_{H_2}) \simeq \frac{d}{2b_{H_2}} \ln \left[\frac{2b_{H_2} N_1}{(1-d)c_1 N_0} \left(\frac{G_0' I_0'}{2\mathcal{R} Z' n} \right)^{1/d} \right] . \tag{B7}$$

These limiting solutions correspond to $G_0'/n \ll 0.019$ cm^3 and $G_0'/n \gg 0.019$ cm^3, respectively. The two limiting solutions can be combined in a simple expression that preserves the limiting solutions, and smoothly transitions from one to the other when $A_V(R_{H_2}) \sim [2b_{H_2}]^{-1} \sim 0.25$:

$$A_V(R_{H_2}) \simeq \frac{d}{2b_{H_2}} \ln \left[1 + \frac{2b_{H_2} N_1}{d(1-d)c_1 N_0} \left(\frac{G_0' I_0'}{2\mathcal{R} Z' n} \right)^{1/d} \right] \tag{B8}$$

Our numerical code uses the Meudon code to solve for the dust extinction and H_2 self-shielding that leads to the H/H_2 transition in a slab. From the code results for $Z' = 1$, we find that for our range of G_0'/n (which extends from 4.2×10^{-3} cm^3 to 0.3 cm^3), $A_V(R_{H_2}) \sim 0.05-1$ and $N_{H_2}(R_{H_2}) \sim 10^{19} - 10^{20}$ cm^{-2}. We fit the self shielding for the critical range 10^{18} cm$^{-2} < N_{H_2} < 10^{20}$ cm^{-2} with $N_1 = 3.6 \times 10^{12}$ cm^{-2} and $d = 0.57$. We fit the dust shielding of the FUV with $b_{H_2} \simeq 2$. In the limited allowed range $0.5 < c_1 < 1$, we find that $c_1 = 0.5$ best fits the numerical results, as expected from the above discussion. Therefore, we obtain the analytic expression

$$A_V(R_{H_2}) \simeq 0.142 \ln \left[1 + 5.2 \times 10^3 Z' \left(\frac{G_0'}{Z' n} \right)^{1.75} \right] , \tag{B9}$$

where n is in cm^{-3} and G_0' references the Draine field. Over the relevant range $4.2 \times 10^{-3} < G_0'/n < 0.3$ (which corresponds to $0.05 < A_V(R_{H_2}) < 1.1$), and for $Z' = 0.5$, 1, and 1.9, we find that this analytic solution matches the numerical code result to better than 5%.

C. Analytic Treatment of A_V(CO)

In our standard runs with relatively low cosmic-ray ionization rates (primary rates $\sim 2 \times 10^{-17}$ s^{-1}), the chemistry of CO from the surface of the cloud to A_V(CO) is dominated by the formation of OH on grain surfaces followed by a chemical chain that leads to CO. The OH abundance is determined by equating the formation of OH on grain surfaces (O + gr $\rightarrow$ OH) to the FUV photodissociation of OH (OH + $h\nu \rightarrow$ O + H):

$$\gamma_1 x_O n^2 = I_{OH}' G_0' e^{-2b_{OH} A_V} x_{OH} n, \tag{C1}$$

where n is the hydrogen nucleus density, $\gamma_1 \simeq 5 \times 10^{-17} Z'$ cm^3 s^{-1} (Hollenbach et al. 2009) is the effective rate coefficient for O atoms colliding and sticking to dust grains (the dust cross section per H nucleus is contained in γ_1), $x_{\rm O} n = n({\rm O})$ is the density of O atoms in the gas, $I'_{\rm OH} = 3.5 \times 10^{-10}$ s^{-1} (Roberge et al. 1991; Woodall et al. 2007) is the (unshielded) photodissociation rate of OH in the local (Draine) interstellar field, G'_0 is the ratio of the incident FUV field to the Draine field, $b_{\rm OH} = 1.7$ is the factor that, multiplied by A_V, gives the effective grain optical depth in the FUV to photons that dissociate OH, $x_{\rm OH} n = n({\rm OH})$ is the OH number density in the gas, and the factor of 2 in the exponential reflects the assumption that a diffuse field incident on a cloud can be approximated by a 1D flux incident at an angle of 60 degrees to the normal. Note that we assume that every atomic O that strikes a grain sticks to the grain, reacts with an H atom, and comes off the grain as OH. Equivalently, it might react with another H atom, form H_2O on the grain surface and photodesorb as either OH or as H_2O, which immediately photodissociates to OH. We derive from eq. (C1):

$$x_{\rm OH} = \frac{\gamma_1 x_{\rm O} n}{I'_{\rm OH} G'_0 e^{-2 b_{\rm OH} A_V}} \tag{C2}$$

Once OH is formed the chemistry proceeds as follows:

$$\rm OH + C^+ \rightarrow CO^+ + H.$$

$$\rm CO^+ + H_2 \rightarrow HCO^+ + H.$$

$$\rm HCO^+ + e \rightarrow CO + H.$$

$$\rm CO + h\nu \rightarrow C + O.$$

The first reaction dominates the formation of CO^+; the second reaction dominates the destruction of CO^+ and the formation of HCO^+; the third reaction dominates the destruction of HCO^+ and the formation of CO; the last reaction dominates the destruction of CO. As a result, every CO^+ that is formed by the first reaction results in a formation of a CO by the third reaction. We can then equate the formation rate of CO (the first reaction) with the destruction rate of CO (the last reaction):

$$\gamma_2 x_{\rm OH} x_{\rm C^+} n^2 = I'_{\rm CO} G'_0 f_{\rm CO} e^{-2 b_{\rm CO} A_V} x_{\rm CO} n, \tag{C3}$$

where $\gamma_2 = 2.9 \times 10^{-9} (T/300 \text{ K})^{-0.33}$ cm^3 s^{-1} (Dubernet et al. 1992; E. Herbst 2006 private communication[7]) is the rate coefficient for OH reacting with C^+ (first reaction), $x_{\rm C^+} n$ is the C^+ gas phase number density, $I'_{\rm CO} = 2.6 \times 10^{-10}$ s^{-1} (Visser et al. 2009) is the unshielded photodissociation rate of CO in the Draine field, $f_{\rm CO}$ is the shielding factor caused by CO

[7]see also http://www.physics.ohio-state.edu/∼eric/research.html

(self-shielding) and H_2, the exponential factor is shielding of CO by dust, $b_{\rm CO} = 3.2$, and $x_{\rm CO}n$ is the number density of CO.

Near $A_V(R_{\rm CO})$, the CO photosphere, we find by fitting to Visser et al. (2009) that

$$f_{\rm CO} = c_{\rm CO}\left[\frac{2N_{\rm CO}}{10^{16}\ {\rm cm}^{-2}}\right]^{-0.60}, \tag{C4}$$

where $c_{\rm CO} = 4.4 \times 10^{-2}$ and where the factor of 2 applies because $N_{\rm CO}$ is the column of CO along a line of sight perpendicular to the surface, whereas our isotropic field is roughly equivalent to a 1D flux incident at an angle of 60 degrees to the surface. The flux then traverses a column $2N_{\rm CO}$ to the point in question (see the discussion of $A_V(R_{\rm H_2})$ in Appendix B).

We substitute equation (C4) and equation (C2) into equation (C3) and integrate both sides of the equation over dz, the perpendicular depth into the cloud, until we reach the CO photosphere, $N_{\rm CO} = 2 \times 10^{16}$ cm^{-2} at $A_V(R_{\rm CO})$. Here we use $ndz = N_0 dA_V$ with $N_0 = 1.9 \times 10^{21}/Z'$ cm^{-2} and $x_{\rm CO}ndz = dN_{\rm CO}$:

$$\int_0^{A_V(R_{\rm CO})}\left[\frac{\gamma_1\gamma_2 x_{\rm O}x_{\rm C^+}n^2}{I'_{\rm OH}G'_0}\right]e^{2(b_{\rm OH}+b_{\rm CO})A_V}dA_V = \tag{C5}$$

$$\int_0^{2\times10^{16}\ {\rm cm}^{-2}} I'_{\rm CO}G'_0\left[\frac{2N_{\rm CO}}{10^{16}\ {\rm cm}^{-2}}\right]^{-0.60}dN_{\rm CO}. \tag{C6}$$

Assuming that the density is constant from the surface to $A_V(R_{\rm CO})$ and that the carbon is entirely C^+ ($x_{\rm C^+} = x_{\rm C}$), we solve for $A_V({\rm CO})$:

$$A_V(R_{\rm CO}) = \frac{1}{2(b_{\rm OH}+b_{\rm CO})}\ln\left[\frac{4.35\times10^{16}c_{\rm CO}(b_{\rm OH}+b_{\rm CO})I'_{\rm OH}I'_{\rm CO}G'^2_0}{N_0\gamma_1\gamma_2x_{\rm O}x_{\rm C}n^2}+1\right], \tag{C7}$$

where $x_{\rm O} \simeq 3.2\times10^{-4}Z'$ is the gas phase abundance of atomic O, $x_{\rm C} \simeq (1.6\times10^{-4})Z'$ is the gas phase abundance of atomic carbon, and Z' is the metallicity relative to solar. We find this analytic solution is good to within 15% except for the lowest Z' and G'_0 model ($Z' = 0.5$, $G'_0 = 3$), where the fit is good to within 25%.

REFERENCES

Abdo, A. A., et al. 2010, ApJ, 710, 133

Andersson, B.-G., & Wannier, P. G. 1993, ApJ, 402, 585

Andersson, B.-G., Wannier, P. G., & Morris, M. 1991, ApJ, 366, 464

Audit, E., & Hennebelle, P. 2010, A&A, 511, A76

Badnell, N. R. 2006, ApJS, 167, 334

Bloemen, J. B. G. M., et al. 1986, A&A, 154, 25

Bohlin, R. C., Savage, B. D., & Drake, J. F. 1978, ApJ, 224, 132

Bolatto, A. D., Leroy, A. K., Rosolowsky, E., Walter, F., & Blitz, L. 2008, ApJ, 686, 948

Burgh, E. B., France, K., & McCandliss, S. R. 2007, ApJ, 658, 446

Cubick, M., Stutzki, J., Ossenkopf, V., Kramer, C., Röllig, M. 2008, A&A, 488, 623

Dame, T. M., Hartmann, D., & Thaddeus, P. 2001, ApJ, 547, 792

Draine, B. T. 1978, ApJS, 36, 595

Draine, B. T., & Bertoldi, F. 1996, ApJ, 468, 269

Dubernet, M. L., Gargaud, M., & McCarroll, R. 1992, A&A, 259, 373

Dufour, R. J. 1984, Structure and Evolution of the Magellanic Clouds, 108, 353

Federman, S. R., Huntress, W. T., Jr., & Prasad, S. S. 1990, ApJ, 354, 504

Federman, S. R., Rawlings, J. M. C., Taylor, S. D., & Williams, D. A. 1996, MNRAS, 279, L41

Gillmon, K., & Shull, J. M. 2006, ApJ, 636, 908

Glover, S. C. O., & Mac Low, M.-M. 2007, ApJ, 659, 1317

Goldsmith, P. F., Heyer, M., Narayanan, G., Snell, R., Li, D., & Brunt, C. 2008, ApJ, 680, 428

Grenier, I. A., Casandjian, J.-M., & Terrier, R. 2005, Science, 307, 1292

Habing, H. J. 1968, Bull. Astron. Inst. Netherlands, 19, 421

Heyer, M. H., & Brunt, C. M. 2004, ApJ, 615, L45

Heyer, M., Krawczyk, C., Duval, J., & Jackson, J. M. 2009, ApJ, 699, 1092

Hollenbach, D., Kaufman, M. J., Bergin, E. A., & Melnick, G. J. 2009, ApJ, 690, 1497

Hollenbach, D. J., & Tielens, A. G. G. M. 1999, Reviews of Modern Physics, 71, 173

Indriolo, N., Geballe, T. R., Oka, T., & McCall, B. J. 2007, ApJ, 671, 1736

Israel, F. P. 1997, A&A, 328, 471

Joulain, K., Falgarone, E., Des Forets, G. P., & Flower, D. 1998, A&A, 340, 241

Kaufman, M. J., Wolfire, M. G., & Hollenbach, D. J. 2006, ApJ, 644, 283

Kaufman, M. J., Wolfire, M. G., Hollenbach, D. J., & Luhman, M. L. 1999, ApJ, 527, 795

Krumholz, M. R., McKee, C. F., & Tumlinson, J. 2009, ApJ, 693, 216

Krumholz, M. R., McKee, C. F., & Tumlinson, J. 2008, ApJ, 689, 865

Larson, R. B. 1981, MNRAS, 194, 809

Le Petit, F., Nehmé, C., Le Bourlot, J., & Roueff, E. 2006, ApJS, 164, 506

Leroy, A., Bolatto, A., Stanimirovic, S., Mizuno, N., Israel, F., & Bot, C. 2007, ApJ, 658, 1027

Liszt, H. S. 2007, A&A, 476, 291

Lombardi, M., Alves, J., & Lada, C. J. 2006, A&A, 454, 78

McCall, B. J., Geballe, T. R., Hinkle, K. H., & Oka, T. 1999, ApJ, 522, 338

McCall, B. J., et al. 2003, Nature, 422, 500

McKee, C. F., & Krumholz, M. R. 2010, ApJ, 709, 308

McKee, C. F., & Ostriker, E. C. 2007, ARA&A, 45, 565

McKee, C. F., & Williams, J. P. 1997, ApJ, 476, 144

Mizuno, A., Yamaguchi, R., Tachihara, K., Toyoda, S., Aoyama, H., Yamamoto, H., Onishi, T., & Fukui, Y. 2001, PASJ, 53, 1071

Nahar, S. N., & Pradhan, A. K. 1997, ApJS, 111, 339

Neufeld, D. A., Wolfire, M. G., & Schilke, P. 2005, ApJ, 628, 260

Ostriker, E. C., Stone, J. M., & Gammie, C. F. 2001, ApJ, 546, 980

Padoan, P., Jones, B. J. T., & Nordlund, A. P. 1997, ApJ, 474, 730

Parravano, A., Hollenbach, D. J., & McKee, C. F. 2003, ApJ, 584, 797

Piontek, R. A., & Ostriker, E. C. 2007, ApJ, 663, 183

Rachford, B. L., et al. 2002, ApJ, 577, 221

Rathborne, J. M., Johnson, A. M., Jackson, J. M., Shah, R. Y., & Simon, R. 2009, ApJS, 182, 131

Reach, W. T., Koo, B.-C., & Heiles, C. 1994, ApJ, 429, 672

Ridge, N. A., et al. 2006, AJ, 131, 2921

Roberge, W. G., Jones, D., Lepp, S., & Dalgarno, A. 1991, ApJS, 77, 287

Sanders, D. B., Scoville, N. Z., Tilanus, R. P. J., Wang, Z., & Zhou, S. 1993, Back to the Galaxy, 278, 311

Sheffer, Y., Rogers, M., Federman, S. R., Abel, N. P., Gredel, R., Lambert, D. L., & Shaw, G. 2008, ApJ, 687, 1075

Shibai, H., et al. 1991, ApJ, 374, 522

Sofia, U. J., Lauroesch, J. T., Meyer, D. M., & Cartledge, S. I. B. 2004, ApJ, 605, 272

Solomon, P. M., Rivolo, A. R., Barrett, J., & Yahil, A. 1987, ApJ, 319, 730

Sonnentrucker, P., Welty, D. E., Thorburn, J. A., & York, D. G. 2007, ApJS, 168, 58

Sternberg, A. 1988, ApJ, 332, 400

Strong, A. W., & Mattox, J. R. 1996, A&A, 308, L21

Tielens, A. G. G. M., & Hollenbach, D. 1985, ApJ, 291, 722

van Dishoeck, E. F., & Black, J. H. 1986, ApJS, 62, 109

van Dishoeck, E. F., & Black, J. H. 1988, ApJ, 334, 771

Vazquez-Semadeni, E. 1994, ApJ, 423, 681

Visser, R., van Dishoeck, E. F., & Black, J. H. 2009, A&A, 503, 323

Wannier, P. G., Lichten, S. M., & Morris, M. 1983, ApJ, 268, 727

Weingartner, J. C., & Draine, B. T. 2001, ApJ, 548, 296

Williams, J. P., & McKee, C. F. 1997, ApJ, 476, 166

Wolfire, M. G., McKee, C. F., Hollenbach, D., & Tielens, A. G. G. M. 2003, ApJ, 587, 278

Wolfire, M. G., Tielens, A. G. G. M., & Hollenbach, D. 1990, ApJ, 358, 116

Wolfire, M. G., Tielens, A. G. G. M., Hollenbach, D., & Kaufman, M. J. 2008, ApJ, 680, 384

Woodall, J., Agúndez, M., Markwick-Kemper, A. J., & Millar, T. J. 2007, A&A, 466, 1197

Yamamoto, H., Kawamura, A., Tachihara, K., Mizuno, N., Onishi, T., & Fukui, Y. 2006, ApJ, 642, 307

Zsargó, J., & Federman, S. R. 2003, ApJ, 589, 319

Figures

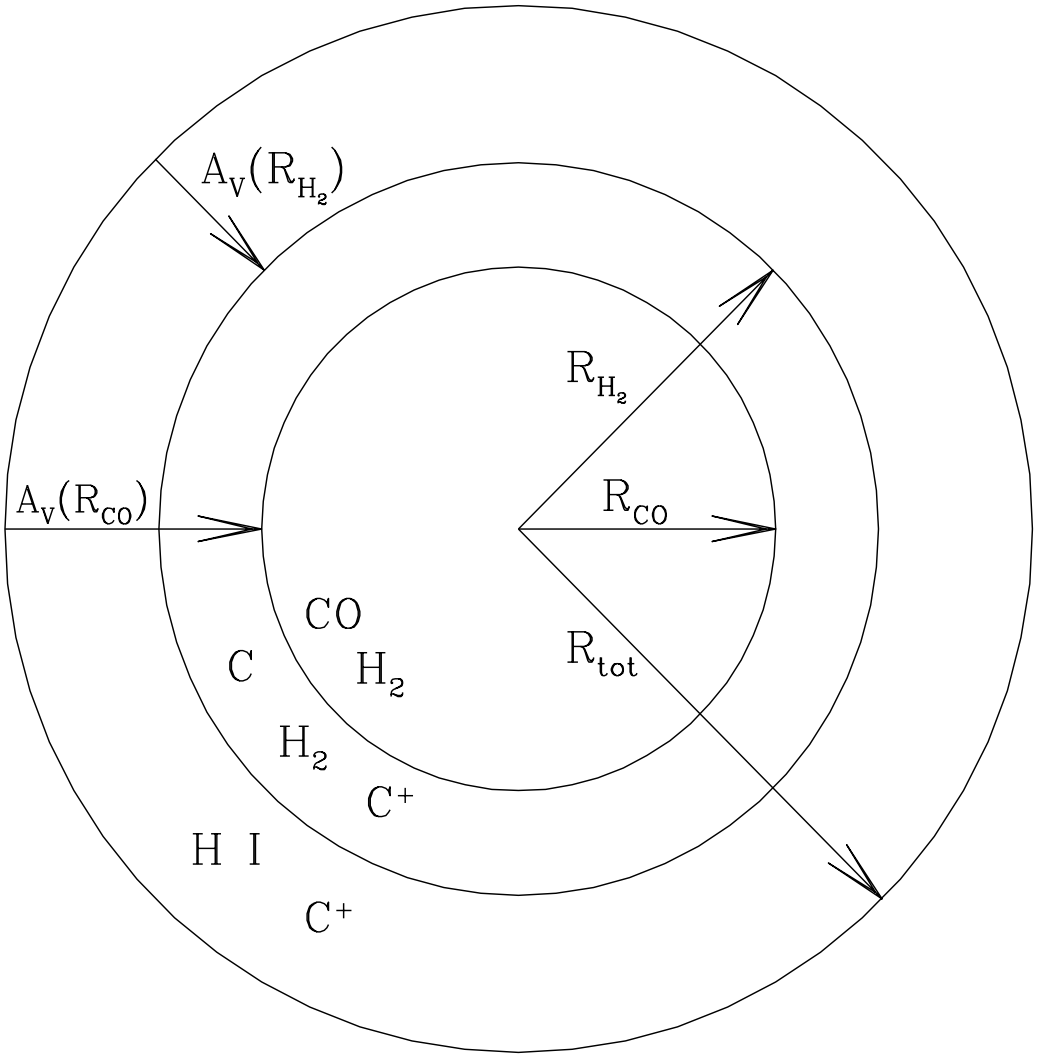

Fig. 1.— Illustration of a model cloud showing the radius $R_{\rm CO}$ of the CO core, the radius $R_{\rm H_2}$ where $2n_{\rm H_2} = n_{\rm HI}$ (equal mass density in H atoms and H_2 molecules), and $R_{\rm tot}$ the total cloud radius. Within $R < R_{\rm CO}$, gas is mainly CO and H_2. Within the range $R_{\rm CO} < R < R_{\rm H_2}$, gas is mainly H_2 whereas the gas phase carbon is mainly C and C^+. Within the range $R_{\rm H_2} < R < R_{\rm tot}$ gas is mainly H I whereas the gas phase carbon is mainly C^+. $A_V(R_{\rm H_2})$ is the optical depth measured from the outer radius to $R_{\rm H_2}$ and $A_V(R_{\rm CO})$ is the optical depth

measured from the outer radius to $R_{\rm CO}$.

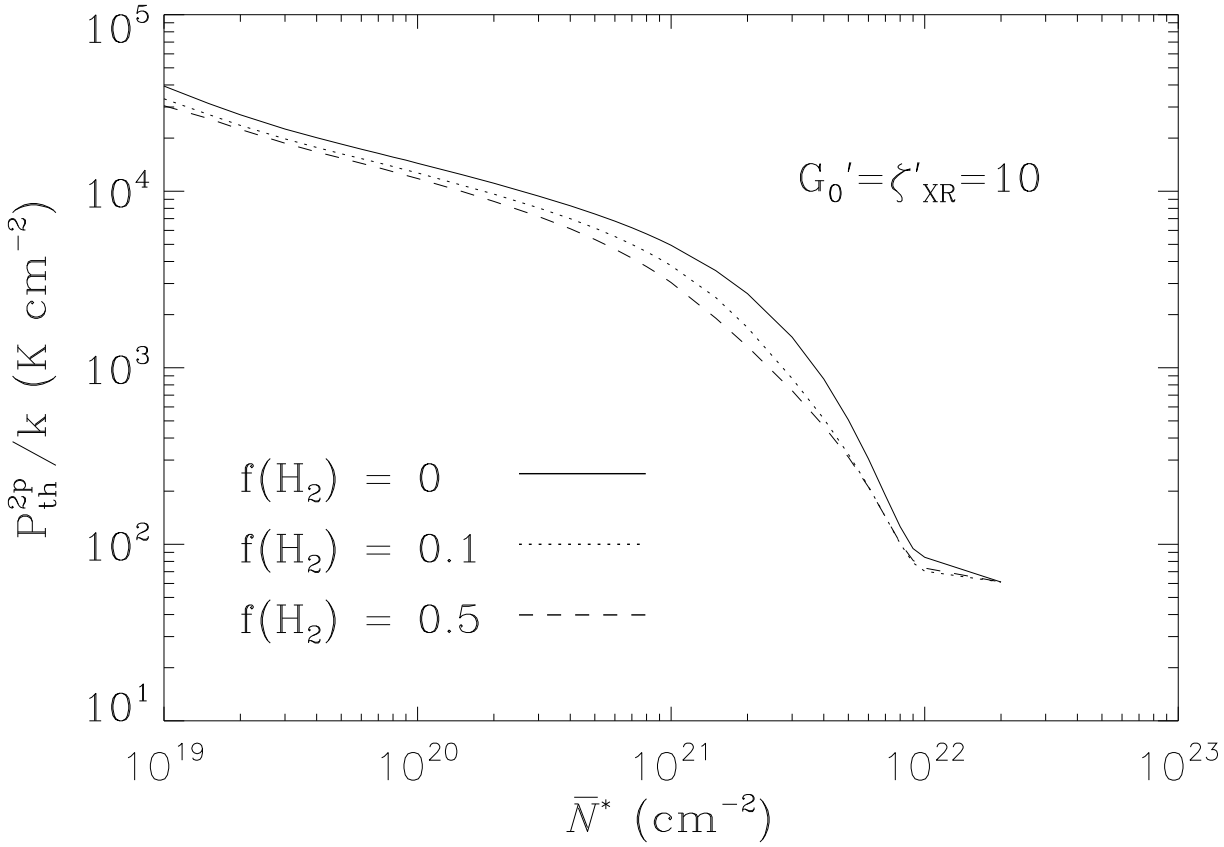

Fig. 2.— Average two-phase thermal pressure $P_{\rm th}^{\rm 2p} = (P_{\rm min}P_{\rm max})^{1/2}$ as a function of total column density from the cloud surface $\bar{N}$ and molecular fraction $f({\rm H_2}) = 2N_{\rm H_2}/N$. The FUV radiation field and soft X-ray/EUV ionization rates are a factor of 10 times higher than local interstellar medium values. Curves are shown for $f({\rm H_2}) = 0$ (*solid curve*), $f({\rm H_2}) = 0.1$ (*dotted curve*), and $f({\rm H_2}) = 0.5$ (*dashed curve*)

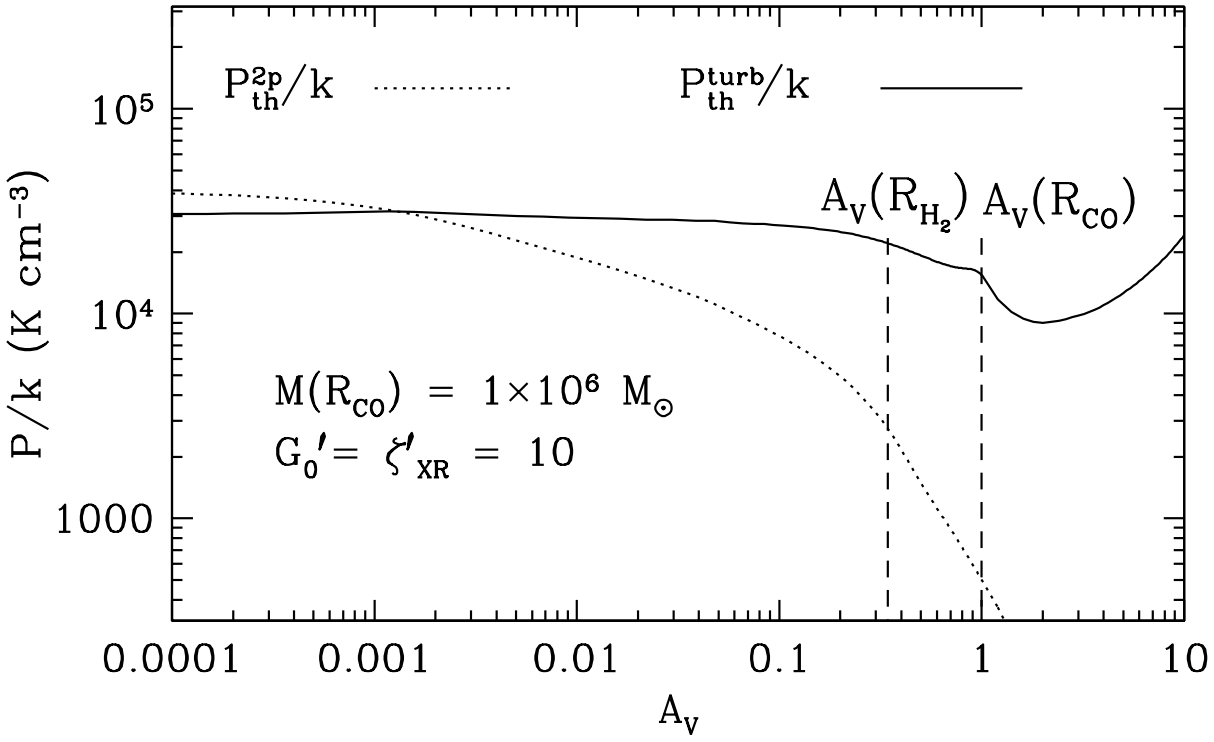
P^{2p}_{th}/k
P^{turb}_{th}/k
$A_V(R_{H_2})$ $A_V(R_{CO})$
$M(R_{CO}) = 1\times10^6\ M_\odot$
$G_0' = \zeta'_{XR} = 10$
P/k (K cm^{-3})
10^5
10^4
1000
0.0001
0.001
0.01
0.1
1
10
A_V

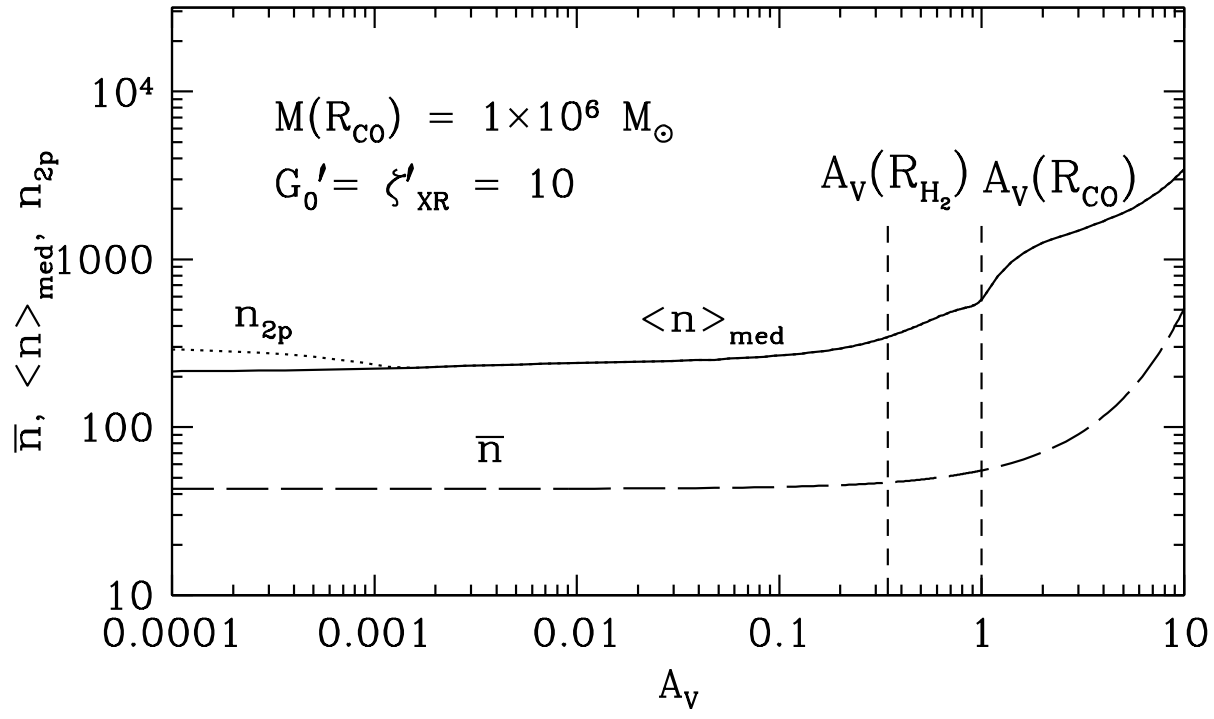
$M(R_{CO}) = 1\times10^6\ M_\odot$
$G_0' = \zeta'_{XR} = 10$
$A_V(R_{H_2})$ $A_V(R_{CO})$
n_{2p}
$<n>_{med}$
$\overline{n}$
$\overline{n}$, $<n>_{med}$, n_{2p}
10^4
1000
100
10
0.0001
0.001
0.01
0.1
1
10
A_V

Fig. 3.— *Top panel:* Thermal pressure as a function of optical depth into the cloud for $M(R_{\rm CO}) = 1 \times 10^6\ M_\odot$, $\bar{N}_{22} = 1.5$, $Z' = 1$, and incident radiation field $G_0' = \zeta_{\rm XR}' = 10$. Curves are shown for two-phase thermal pressure $P_{\rm th}^{\rm 2p}/k = x_t n_{\rm 2p} T/k$ (*dotted curve*) and for turbulent thermal pressure $P_{\rm turb}^{\rm th} = x_t \langle n \rangle_{\rm med} T/k$ (*solid curve*). Optical depths at $A_V(R_{\rm H_2})$ $[n_{\rm H_2}/n = 0.25]$ and $A_V(R_{\rm CO})$ ($\tau_{\rm CO} = 1$) are indicated by vertical dashed lines. Thermal pressure in the turbulent medium dominates at $A_V \gtrsim 0.001$. *Bottom panel:* Density as a function of optical depth into the cloud for $M(R_{\rm CO}) = 1 \times 10^6\ M_\odot$, $\bar{N}_{22} = 1.5$, $Z' = 1$, and incident radiation field $G_0' = \zeta_{\rm XR}' = 10$. Curves are shown for two-phase density $n_{\rm 2p}$, mass-weighted median density $\langle n \rangle_{\rm med}$ in a turbulent density distribution, and volume-averaged density $\bar{n}$. The two-phase density distribution is shown only where two-phase pressure dominates ($A_V \lesssim 0.001$). The local (model) density $n_c = n_{\rm 2p}$ where two-phase pressure dominates and $n_c = \langle n \rangle_{\rm med}$ where turbulent pressure dominates. Optical depths at $A_V(R_{\rm H_2})$ $[n_{\rm H_2}/n = 0.25]$ and $A_V(R_{\rm CO})$ ($\tau_{\rm CO} = 1$) are indicated by vertical dashed lines.

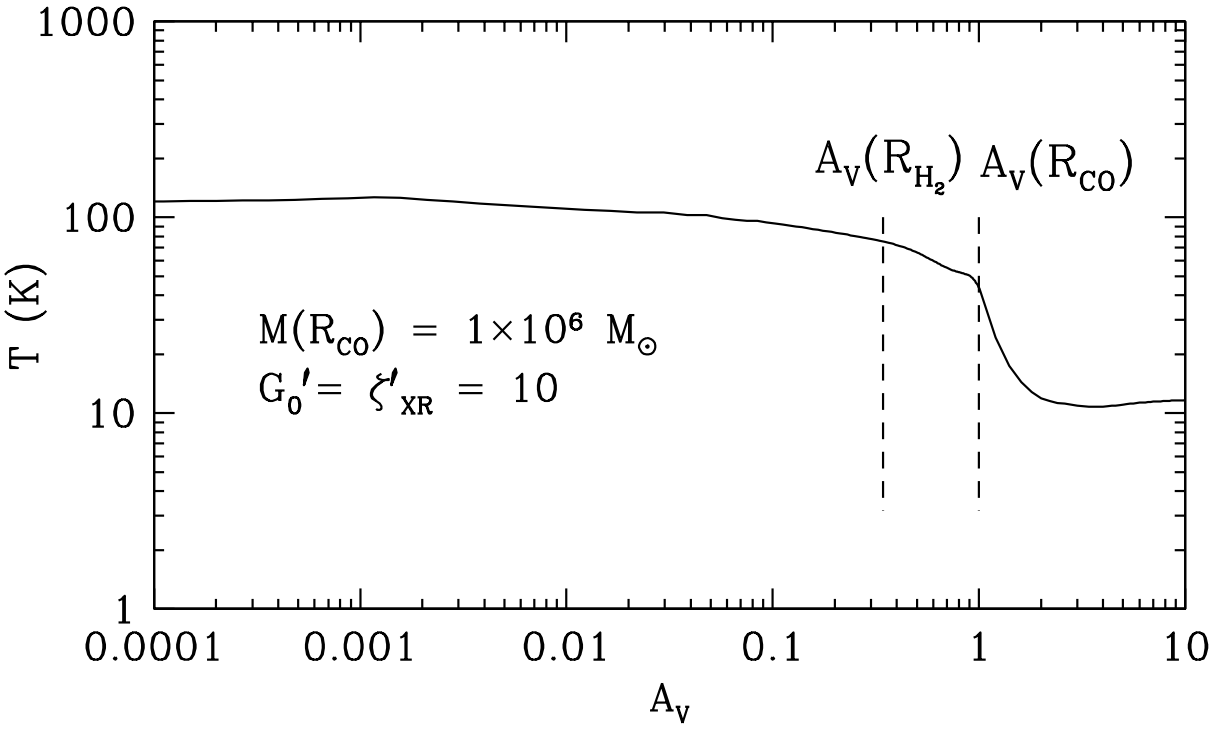
1000
100
10
1
T (K)
0.0001
0.001
0.01
0.1
1
10
A_V
A_V(R_H2) A_V(R_CO)
M(R_CO) = 1×10^6 M_⊙
G_0′ = ζ′_XR = 10

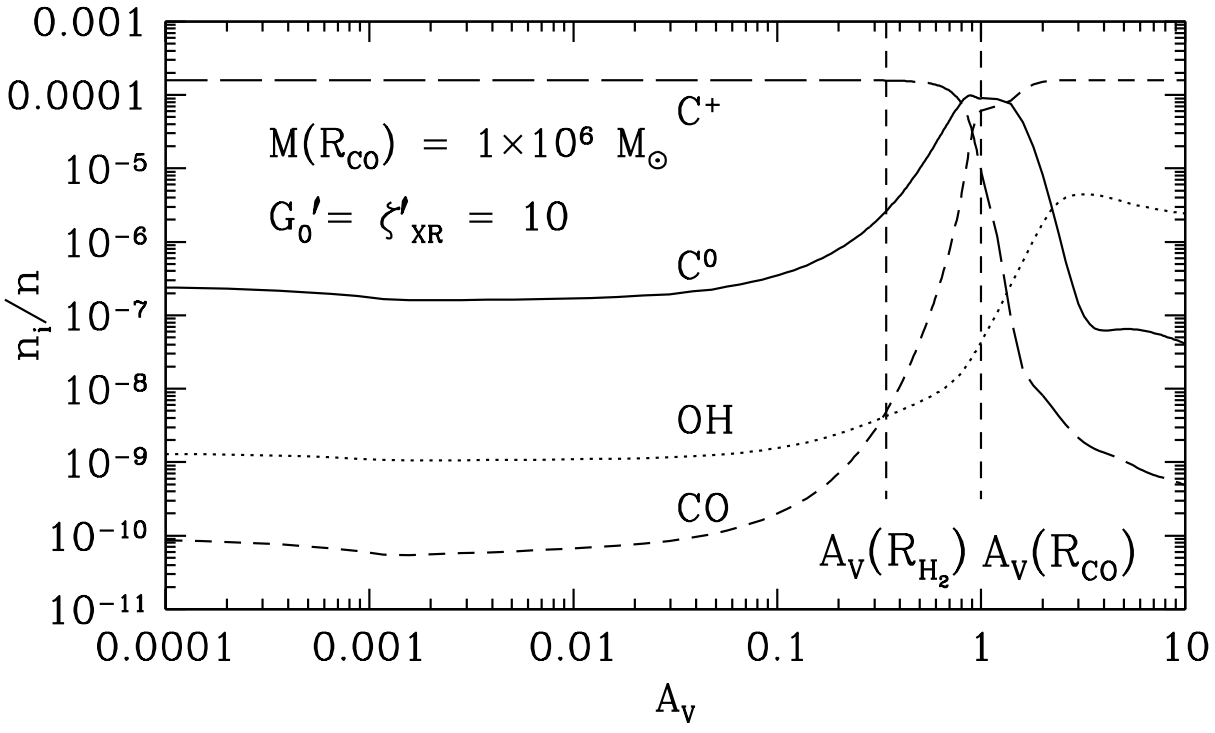
0.001
0.0001
10^-5
10^-6
10^-7
10^-8
10^-9
10^-10
10^-11
n_i/n
0.0001
0.001
0.01
0.1
1
10
A_V
C+
C0
OH
CO
M(R_CO) = 1×10^6 M_⊙
G_0′ = ζ′_XR = 10
A_V(R_H2) A_V(R_CO)

Fig. 4.— *Top panel:* Temperature as a function of optical depth into the cloud for $M(R_{\rm CO}) = 1 \times 10^6\ M_\odot$, $\bar{N}_{22} = 1.5$, $Z' = 1$, and incident radiation field $G_0' = \zeta_{\rm XR}' = 10$. *Bottom panel:* Abundances of C^+ (*long-dash curve*), C^0 (*solid curve*), OH (*dotted curve*), and CO (*short-dash curve*) as functions of optical depth into the cloud for $M(R_{\rm CO}) = 1 \times 10^6\ M_\odot$, $\bar{N}_{22} = 1.5$, $Z' = 1'$, and incident radiation field $G_0' = \zeta_{\rm XR}' = 10$. Note that we do not include freeze out of H_2O on grain surfaces, which would affect OH abundances at $A_V > 3$.

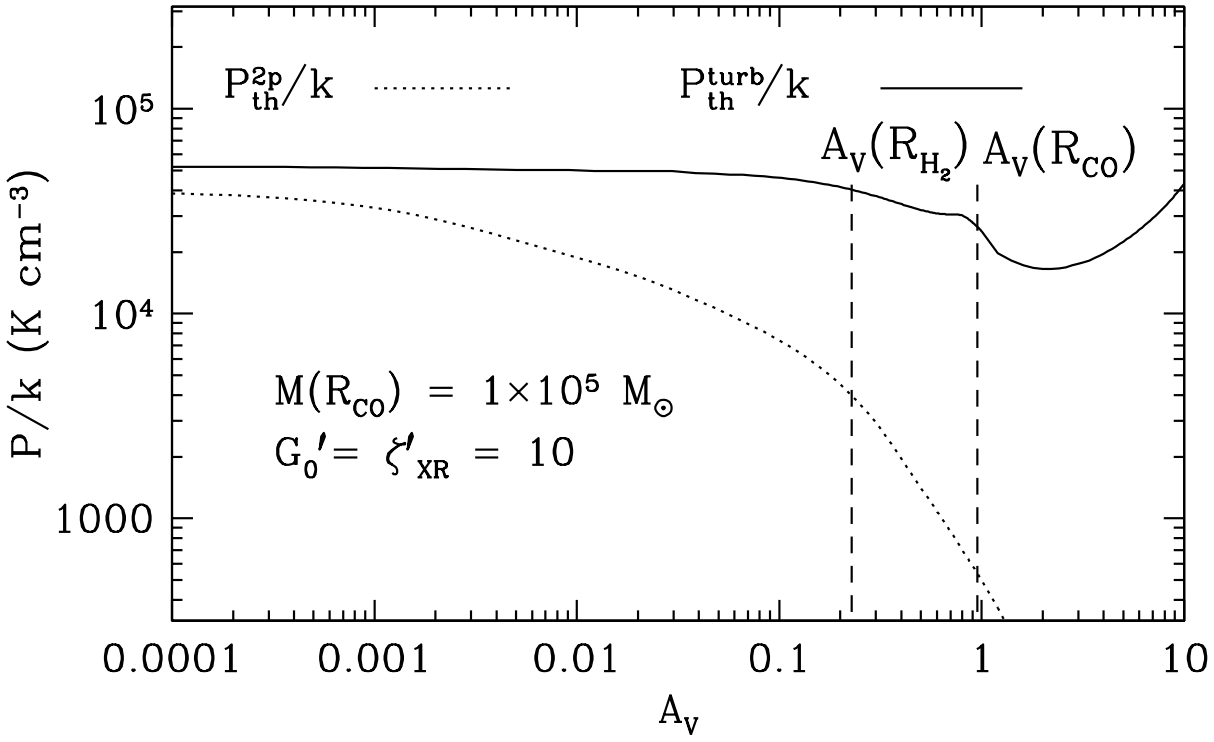
P^{2p}_{th}/k
P^{turb}_{th}/k
$A_V(R_{H_2})$ $A_V(R_{CO})$
$M(R_{CO}) = 1\times10^5\ M_\odot$
$G_0' = \zeta'_{XR} = 10$
P/k (K cm^{-3})
10^5
10^4
1000
0.0001
0.001
0.01
0.1
1
10
A_V

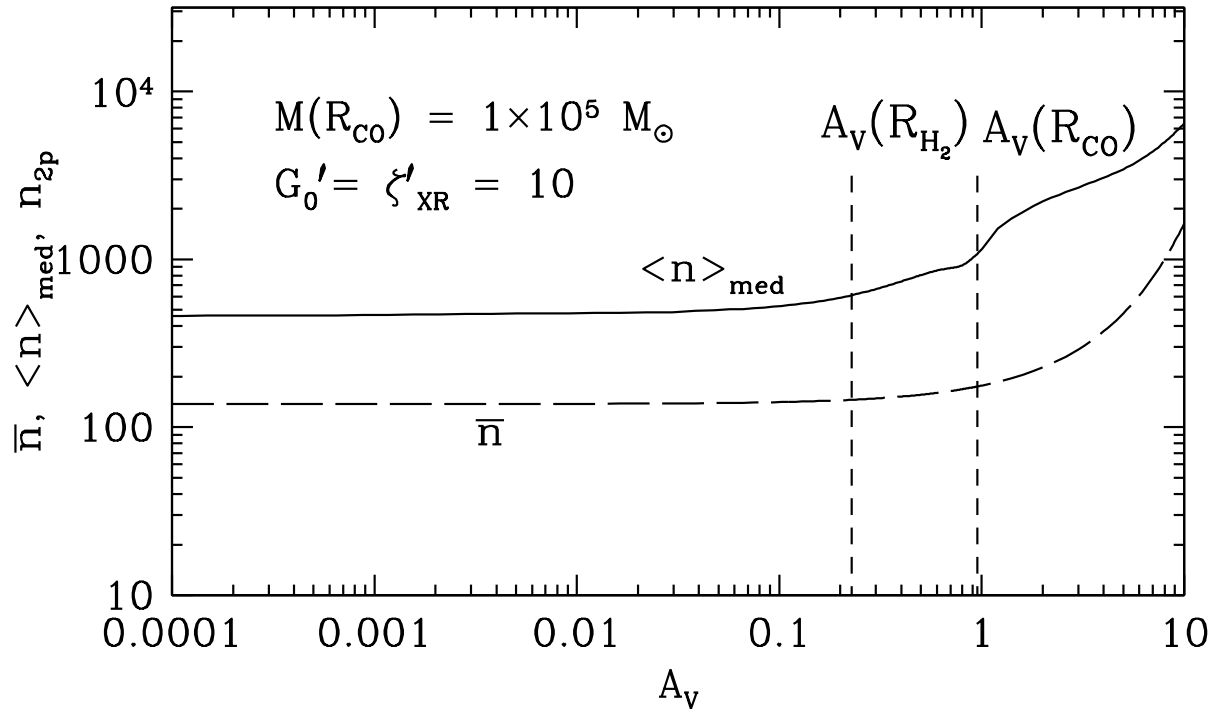
$M(R_{CO}) = 1\times10^5\ M_\odot$
$G_0' = \zeta'_{XR} = 10$
$A_V(R_{H_2})$ $A_V(R_{CO})$
$<n>_{med}$
$\bar{n}$
$\bar{n}$, $<n>_{med}$, n_{2p}
10^4
1000
100
10
0.0001
0.001
0.01
0.1
1
10
A_V

Fig. 5.— *Top panel:* Thermal pressure as a function of optical depth into the cloud for $M(R_{\rm CO}) = 1 \times 10^5\ M_\odot$, $\bar{N}_{22} = 1.5$, $Z' = 1$, and incident radiation field $G_0' = \zeta_{\rm XR}' = 10$. Curves are shown for two-phase thermal pressure $P_{\rm th}^{\rm 2p}/k = x_t n_{\rm 2p} T/k$ (*dotted curve*) and for turbulent thermal pressure $P_{\rm turb}^{\rm th} = x_t \langle n \rangle_{\rm med} T/k$ (*solid curve*). Optical depths at $A_V(R_{\rm H_2})$ $[n_{\rm H_2}/n = 0.25]$ and $A_V(R_{\rm CO})$ ($\tau_{\rm CO} = 1$) are indicated by vertical dashed lines. Thermal pressure in the turbulent medium dominates at all A_V. *Bottom panel:* Density as a function of optical depth into the cloud for $M(R_{\rm CO}) = 1 \times 10^5\ M_\odot$, $\bar{N}_{22} = 1.5$, $Z' = 1$, and incident radiation field $G_0' = \zeta_{\rm XR}' = 10$. Curves are shown for mass-weighted median density $\langle n \rangle_{\rm med}$ in a turbulent density distribution, and volume-averaged density $\bar{n}$. Turbulent pressure dominates at all A_V and thus no two-phase density is shown. The local (model) density $n_c = \langle n \rangle_{\rm med}$. Optical depths at $A_V(R_{\rm H_2})$ $[n_{\rm H_2}/n = 0.25]$ and $A_V(R_{\rm CO})$ ($\tau_{\rm CO} = 1$) are indicated by vertical dashed lines.

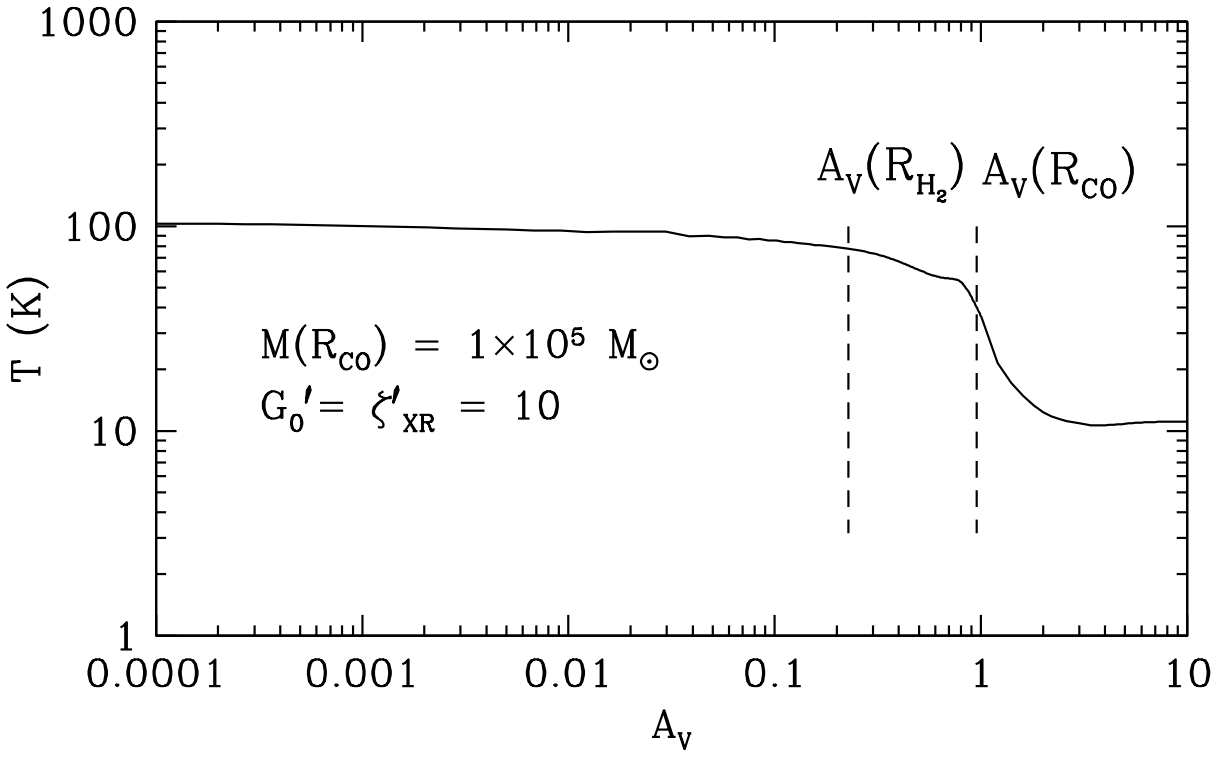
1000
100
10
1
T (K)
$A_V(R_{H_2})$ $A_V(R_{CO})$
$M(R_{CO}) = 1\times10^5\ M_\odot$
$G_0' = \zeta'_{XR} = 10$
0.0001
0.001
0.01
0.1
1
10
A_V

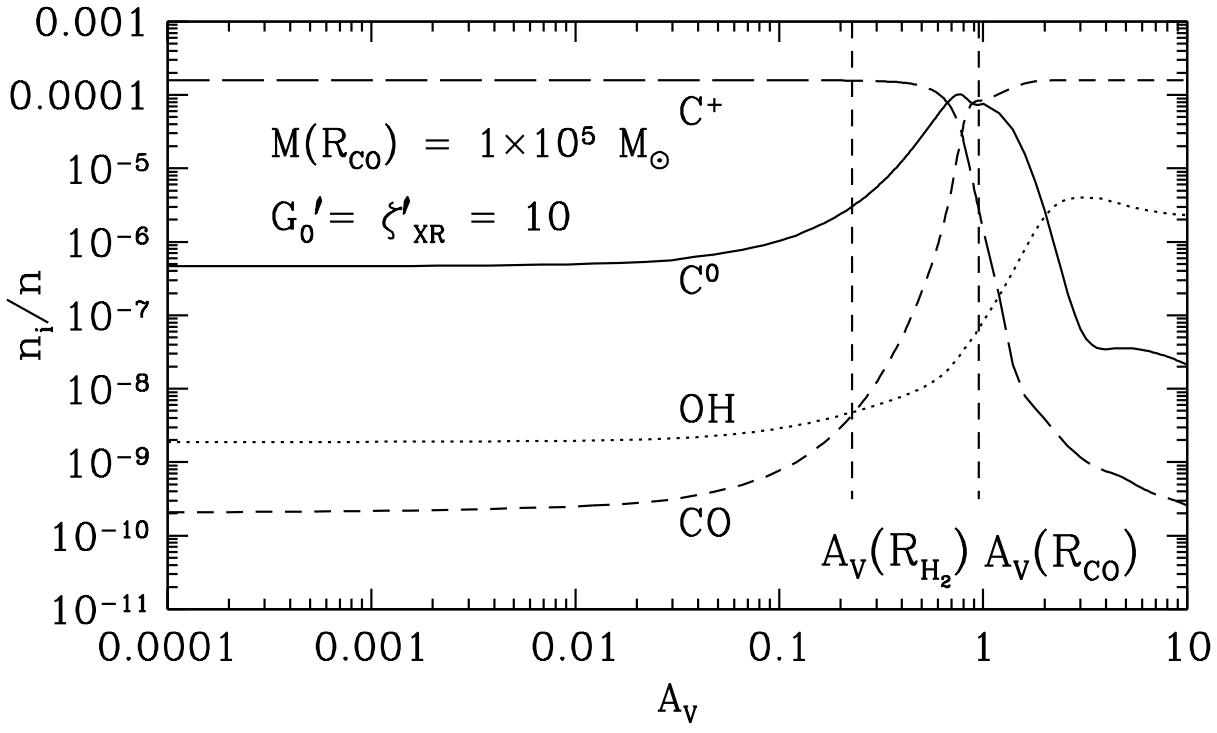
0.001
0.0001
10^{-5}
10^{-6}
10^{-7}
10^{-8}
10^{-9}
10^{-10}
10^{-11}
n_i/n
C^+
$M(R_{CO}) = 1\times10^5\ M_\odot$
$G_0' = \zeta'_{XR} = 10$
C^0
OH
CO
$A_V(R_{H_2})$ $A_V(R_{CO})$
0.0001
0.001
0.01
0.1
1
10
A_V

Fig. 6.— *Top panel:* Temperature as a function of optical depth into the cloud for $M(R_{\rm CO}) = 1 \times 10^5\ M_\odot$, $\bar{N}_{22} = 1.5$, $Z' = 1$, and incident radiation field $G_0' = \zeta_{\rm XR}' = 10$. *Bottom panel:* Abundances of C^+ (*long-dash curve*), C^0 (*solid curve*), OH (*dotted curve*), and CO (*short-dash curve*) as functions of optical depth into the cloud for $M(R_{\rm CO}) = 1 \times 10^5\ M_\odot$, $\bar{N}_{22} = 1.5$, and incident radiation field $G_0' = \zeta_{\rm XR}' = 10$. Note that we do not include freeze out of H_2O on grain surfaces, which would affect OH abundances at $A_V > 3$.

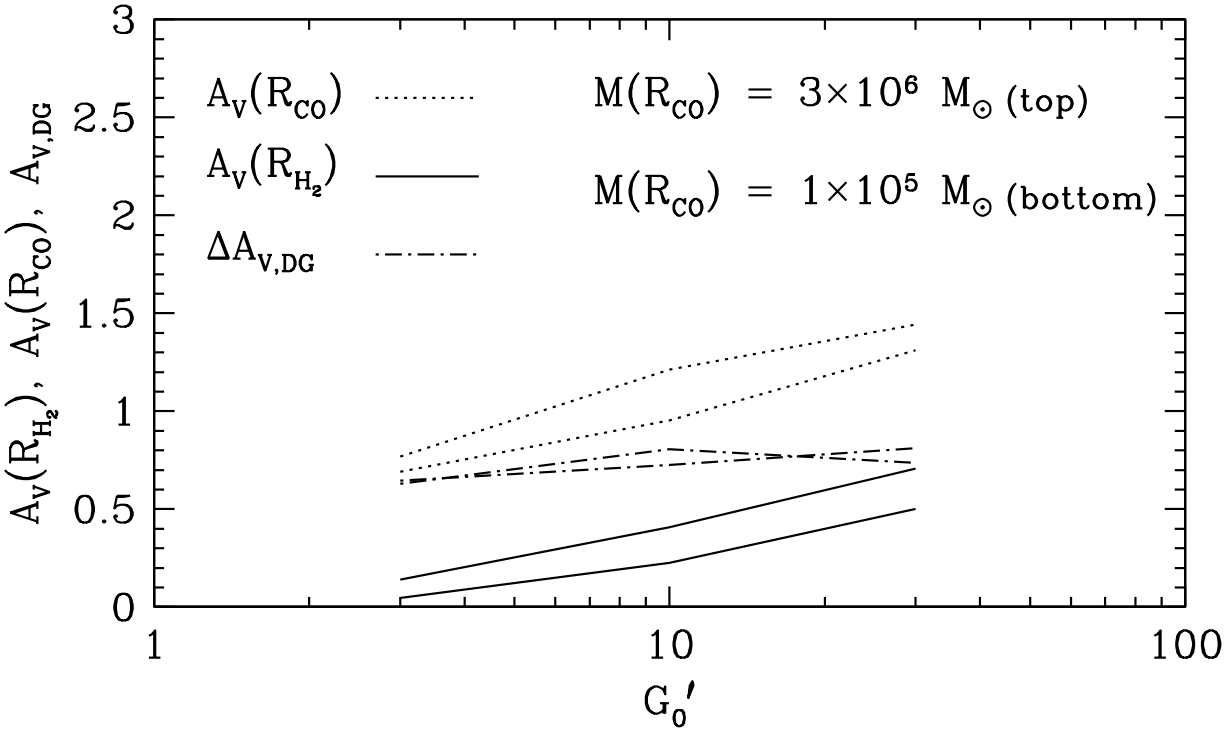
$A_V(R_{CO})$
$A_V(R_{H_2})$
$\Delta A_{V,DG}$
$M(R_{CO}) = 3\times10^6\ M_\odot$ (top)
$M(R_{CO}) = 1\times10^5\ M_\odot$ (bottom)
$A_V(R_{H_2})$, $A_V(R_{CO})$, $A_{V,DG}$
G_0'

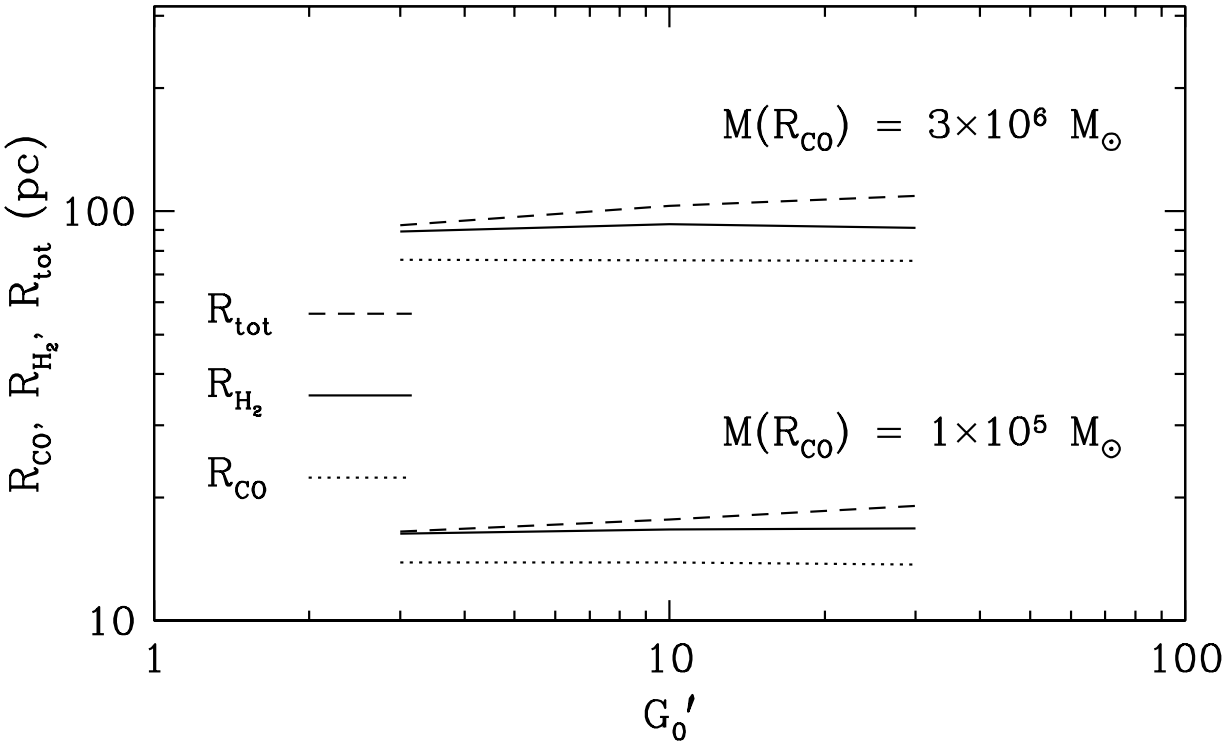
$M(R_{CO}) = 3\times10^6\ M_\odot$
$M(R_{CO}) = 1\times10^5\ M_\odot$
R_{tot}
R_{H_2}
R_{CO}
R_{CO}, R_{H_2}, R_{tot} (pc)
G_0'

Fig. 7.— *Top panel:* Optical depth as a function of cloud mass, $M(R_{\rm CO})$, and incident radiation field, $G_0' = G_0/1.7$. Curves are shown for $\bar{N}_{22} = 1.5$, $Z' = 1$, and two cloud masses, $M(R_{\rm CO}) = 3\times10^6\ M_\odot$ and $M(R_{\rm CO}) = 1\times10^5\ M_\odot$. The optical depth from the cloud surface $R_{\rm tot}$ to $R_{\rm CO}$ is $A_V(R_{\rm CO})$ (*dotted curve*) and the optical depth from the cloud surface $R_{\rm tot}$ to $R_{\rm H_2}$ is $A_V(R_{\rm H_2})$ (*solid curve*). Also shown is $\Delta A_{V,\,\rm DG} = A_V(R_{\rm CO}) - A_V(R_{\rm H_2})$ (*dash-dot curve*) *Bottom panel:* Cloud radii $R_{\rm tot}$ (*dashed curve*), $R_{\rm H_2}$ (*solid curve*), and $R_{\rm CO}$ (*dotted curve*) are shown as functions of cloud mass $M(R_{\rm CO})$ and incident radiation field normalized to the local interstellar field, $G_0' = G_0/1.7$. Curves are shown for $\bar{N}_{22} = 1.5$, $Z' = 1$, and two cloud masses $M(R_{\rm CO}) = 3\times10^6\ M_\odot$ and $M(R_{\rm CO}) = 1\times10^5\ M_\odot$. The radius $R_{\rm H_2}$ is where half the nuclei are in H_2 ($n_{\rm H_2}/n_c = 0.25$), and the radius $R_{\rm CO}$ is where $\tau_{\rm CO} = 1$.

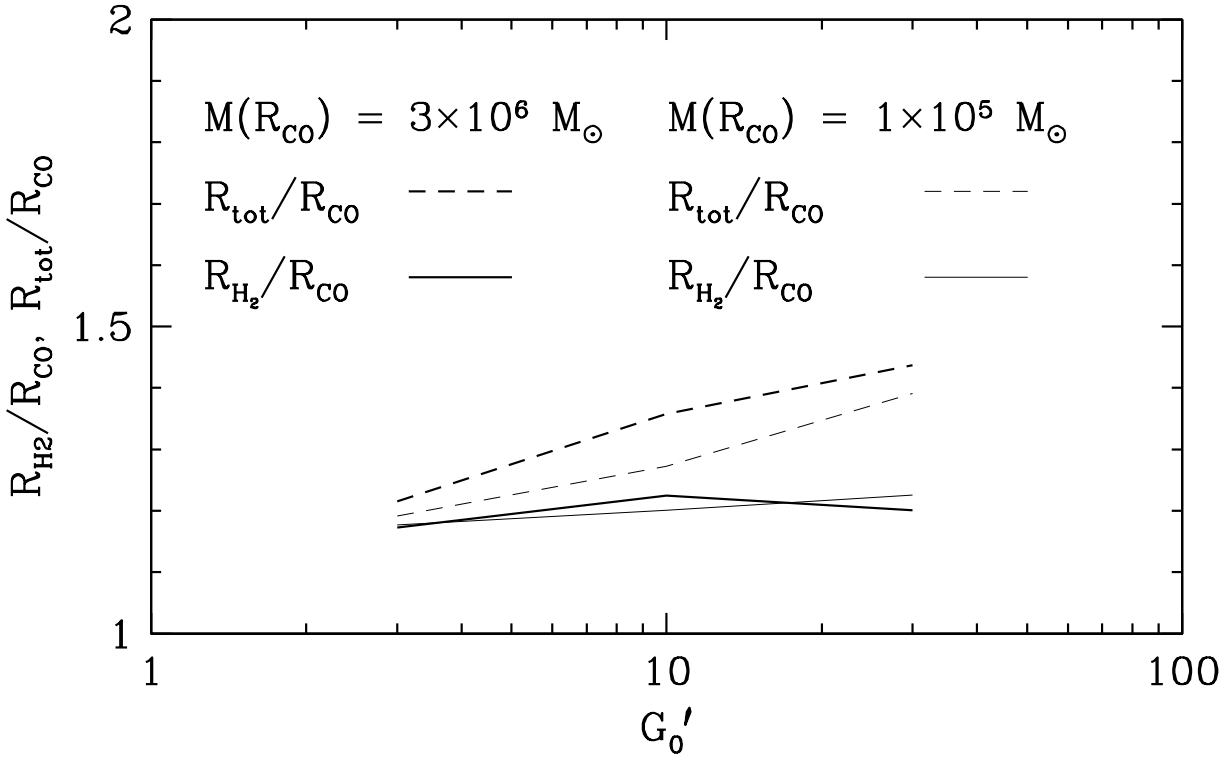
M(R_CO) = 3×10^6 M_⊙
R_tot/R_CO
R_H2/R_CO
M(R_CO) = 1×10^5 M_⊙
R_tot/R_CO
R_H2/R_CO
R_H2/R_CO, R_tot/R_CO
G_0′
2
1.5
1
1
10
100

Fig. 8.— Ratio of cloud radii $R_{\rm tot}/R_{\rm CO}$ (*dashed curve*), and $R_{\rm H_2}/R_{\rm CO}$ (*solid curve*) are shown as functions of cloud mass $M(R_{\rm CO})$ and incident radiation field normalized to the local interstellar field, $G_0' = G_0/1.7$. Curves are shown for $\bar{N}_{22} = 1.5$, $Z' = 1$, and two cloud masses $M(R_{\rm CO}) = 3 \times 10^6\ M_\odot$ (*thick curve*) and $M(R_{\rm CO}) = 1 \times 10^5\ M_\odot$ (*thin curve*). The radius $R_{\rm H_2}$ is where half the nuclei are in H_2 ($n_{\rm H_2}/n_c = 0.25$), and the radius $R_{\rm CO}$ is where $\tau_{\rm CO} = 1$. For $M(R_{\rm CO}) = 3 \times 10^6\ M_\odot$, $R_{\rm CO} = 75.4$ pc and for $M(R_{\rm CO}) = 1 \times 10^5\ M_\odot$, $R_{\rm CO} = 13.8$ pc.

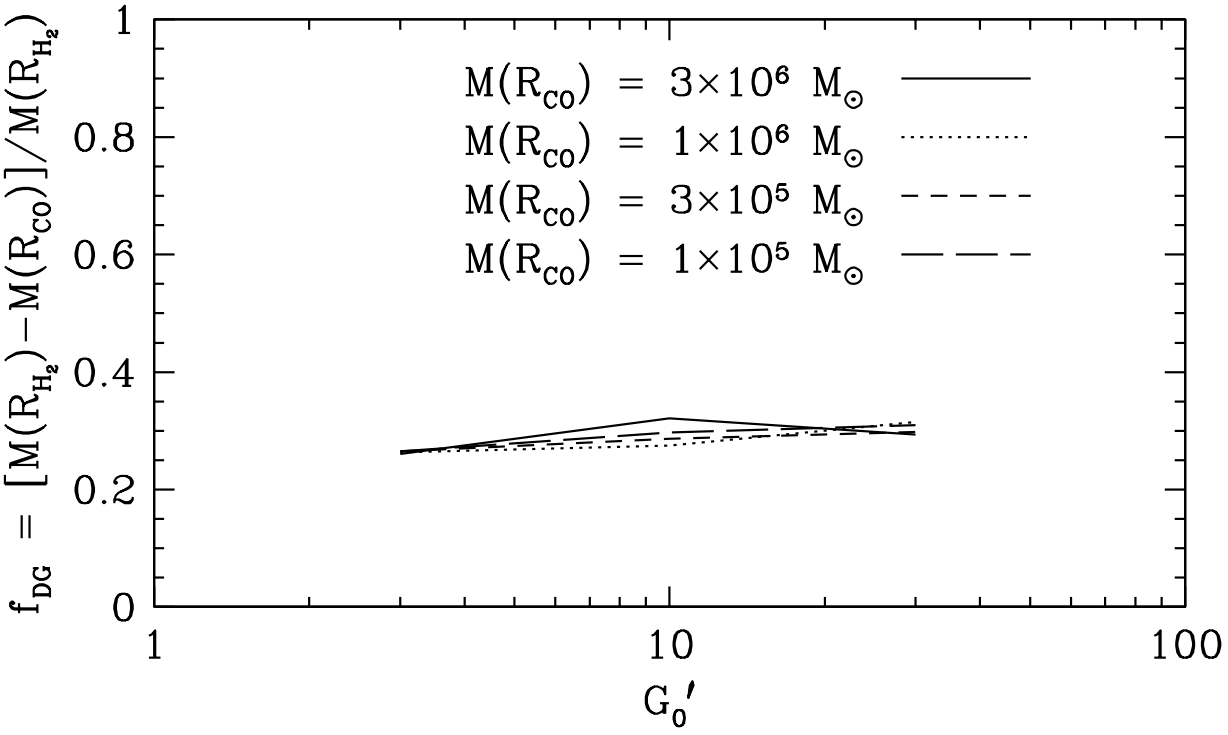
M(R_CO) = 3×10^6 M_⊙
M(R_CO) = 1×10^6 M_⊙
M(R_CO) = 3×10^5 M_⊙
M(R_CO) = 1×10^5 M_⊙
f_DG = [M(R_H2) − M(R_CO)]/M(R_H2)
G_0′
0
0.2
0.4
0.6
0.8
1
1
10
100

Fig. 9.— Dark gas fraction $f_{\rm DG} = [M(R_{\rm H_2}) - M(R_{\rm CO})]/M(R_{\rm H_2})$ versus incident radiation field normalized to the local interstellar field, $G_0' = G_0/1.7$. Curves are shown for $\bar{N}_{22} = 1.5$, $Z' = 1$, and cloud masses $M(R_{\rm CO}) = 3 \times 10^6\ M_\odot$ (*solid curve*), $1 \times 10^6\ M_\odot$ (*dotted curve*), $3 \times 10^5\ M_\odot$ (*short-dash curve*), and $1 \times 10^5\ M_\odot$ (*long-dash curve*).

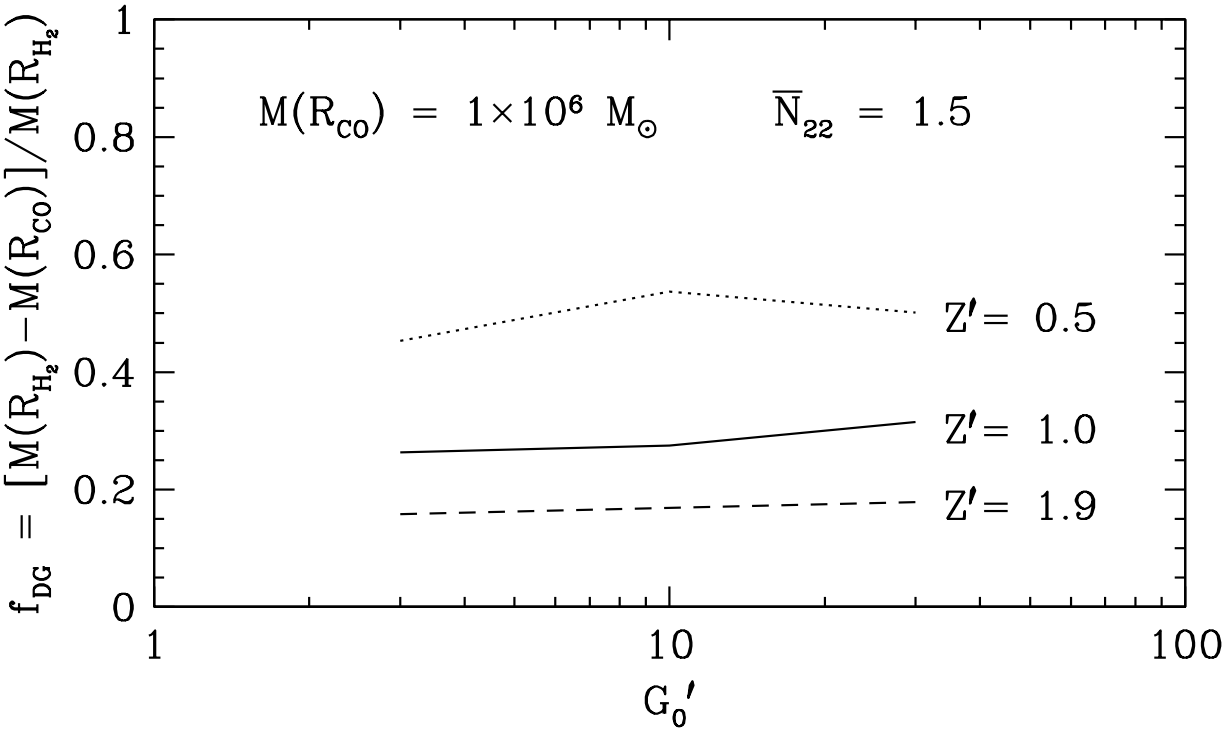
M(R_CO) = 1×10⁶ M⊙
N̄22 = 1.5
Z′= 0.5
Z′= 1.0
Z′= 1.9
f_DG = [M(R_H2) − M(R_CO)]/M(R_H2)
G0′
0
0.2
0.4
0.6
0.8
1
1
10
100

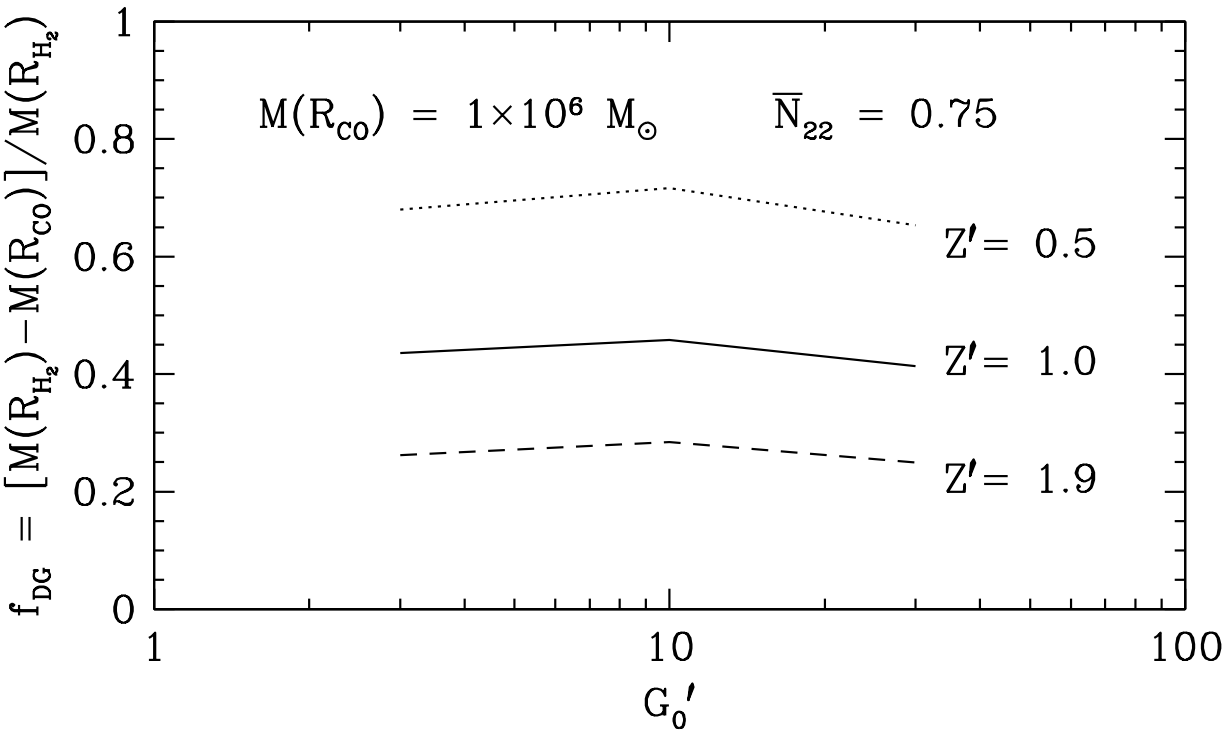
M(R_CO) = 1×10⁶ M⊙
N̄22 = 0.75
Z′= 0.5
Z′= 1.0
Z′= 1.9
f_DG = [M(R_H2) − M(R_CO)]/M(R_H2)
G0′
0
0.2
0.4
0.6
0.8
1
1
10
100

Fig. 10.— *Top panel:* Dark gas fraction $f_{\rm DG} = [M(R_{\rm H_2}) - M(R_{\rm CO})]/M(R_{\rm H_2})$ versus incident radiation field normalized to the local interstellar field, $G_0' = G_0/1.7$. Curves are shown for constant mean column density $\bar{N}_{22} = 1.5$ and metallicities $Z' = 1.9$ (*dashed curve*), $Z' = 1$ (*solid curve*), $Z' = 0.5$ (*dotted curve*). *Bottom panel:* Same as top panel for $\bar{N}_{22} = 0.75$.

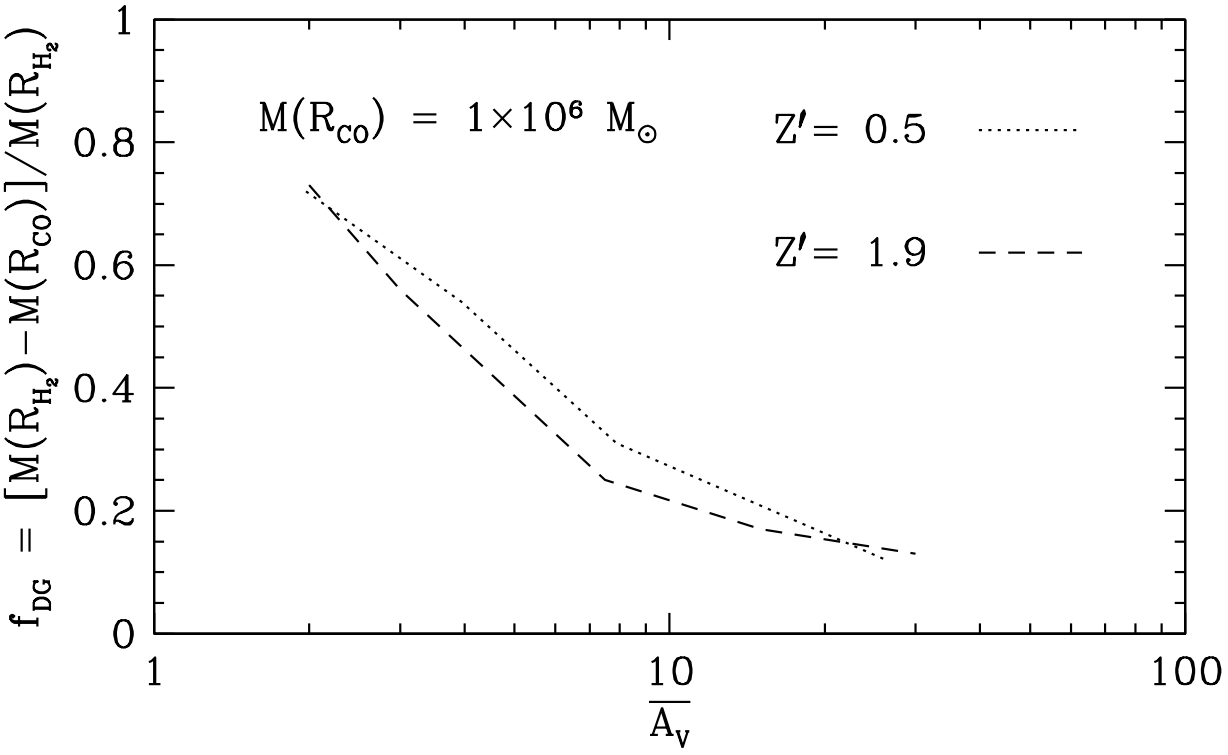
$f_{DG} = [M(R_{H_2}) - M(R_{CO})]/M(R_{H_2})$
1
0.8
0.6
0.4
0.2
0
1
10
100
$\overline{A_V}$
$M(R_{CO}) = 1\times10^6\ M_\odot$
$Z' = 0.5$
$Z' = 1.9$

Fig. 11.— *Top panel:* Dark gas fraction $f_{\rm DG} = [M(R_{\rm H_2}) - M(R_{\rm CO})]/M(R_{\rm H_2})$ as a function of the mean visual extinction through the cloud $\bar{A}_V = 5.26 Z' \bar{N}_{22}$. Curves are shown for constant cloud mass $M(R_{\rm CO}) = 1 \times 10^6\ M_\odot$, $G_0' = 10$, and metallicities $Z' = 1.9$ (*dashed curve*), $Z' = 0.5$ (*dotted curve*). Clouds of higher $\bar{A}_V$ have less surface dark gas relative to the CO interiors.